*J. Fluid Mech.* (2013), *vol.* 724, *pp.* 36–68.  
doi:10.1017/jfm.2013.141

# Flame front/turbulence interaction for syngas fuels in the thin reaction zones regime: turbulent and stretched laminar flame speeds at elevated pressures and temperatures

**S. Daniele[1],†, J. Mantzaras[1], P. Jansohn[1], A. Denisov[1] and K. Boulouchos[2]**

[1]Paul Scherrer Institute (PSI), Combustion Research Laboratory, CH-5232 Villigen PSI, Switzerland

[2]Swiss Federal Institute of Technology (ETH) Aerothermochemistry and Combustion Systems Laboratory, Sonneggstrasse 3, CH-8092 Zürich, Switzerland

(Received 23 November 2011; revised 18 February 2013; accepted 5 March 2013; first published online 29 April 2013)

Experiments were performed in dump-stabilized axisymmetric flames to assess turbulent flame speeds ($S_T$) and mean flamelets speeds (stretched laminar flame speeds, $S_{L,k}$). Fuels with significantly different thermodiffusive properties have been investigated, ranging from pure methane to syngas ($H_2$–CO blends) and pure hydrogen, while the pressure was varied from 0.1 to 1.25 MPa. Flame front corrugation was measured with planar laser-induced fluorescence (PLIF) of the OH radical, while turbulence quantities were determined with particle image velocimetry (PIV). Two different analyses based on mass balance were performed on the acquired flame images. The first method assessed absolute values of turbulent flame speeds and the second method, by means of an improved fractal methodology, provided normalized turbulent flame speeds ($S_T/S_{L,k}$). Deduced average Markstein numbers exhibited a strong dependence on pressure and hydrogen content of the reactive mixture. It was shown that preferential-diffusive-thermal (PDT) effects acted primarily on enhancing the stretched laminar flame speeds rather than on increasing the flame front corrugations. Interaction between flame front and turbulent eddies measured by the fractal dimension was shown to correlate with the eddy temporal activity.

**Key words:** flames, reacting flows, turbulent reacting flows

## 1. Introduction

Within the gas-turbine-based power-generation technologies, there is nowadays increased interest in integrated gasification combined cycle (IGCC) power plants, for reasons of security in fuel supply and optimization in energy use. These plants offer a big potential for clean electricity production with reduced $CO_2$ emissions when operated in the lean premixed combustion mode and when carbon capture technology is applied (Hoffmann *et al.* 2009). Via gasification, IGCC concepts convert solid and liquid hydrocarbons (biomasses, oil, coal, tars, etc.) into a gaseous fuel for gas-turbine-based power generation. The fuel obtained from the gasification process is

† Email address for correspondence: salvatore.daniele@fhnw.ch

conventionally termed syngas. It can be considered as a gaseous mixture containing mostly hydrogen ($H_2$) and carbon monoxide (CO), and the chemical composition varies according to the specific feedstock (e.g. biomass, coal, tar, etc.). It is commonly diluted with inert gases such as nitrogen ($N_2$), steam ($H_2O$) or carbon dioxide ($CO_2$), depending on the gasification process.

Lean premixed combustion is considered as the state-of-the-art technology in stationary gas turbines for highly efficient and low-emission power generation with natural gas fuel. Therein, the latest precombustion $CO_2$ capture technologies aim at efficiently reforming the natural gas fuel to syngas (Tock & Marechal 2012). Therefore, the fundamental properties of syngases need to be investigated for premixed flames under gas-turbine-like operating conditions.

The combustion properties of syngases are mainly determined by their specific $H_2$ and CO content and are generally characterized by very high laminar flame speeds, a wide range of flammability limits and short ignition delay times (Chaos & Dryer 2008; Sung & Law 2008; Daniele *et al.* 2011), which all contribute to a high risk of autoignition and flashback. In addition to the combustion characteristics, the physical properties of $H_2$ are also very different from those of natural gas. For example, the density of $H_2$ is an order of magnitude smaller than that of natural gas, resulting in increased volumetric flow rate requirements for the turbine, and at the same time the molecular diffusivity of $H_2$ is substantially higher, leading to thermal/diffusive imbalance effects during combustion.

When referring to stable and safe lean premixed gas turbine combustion, one of the most important parameters is the turbulent burning velocity, $S_T$. This property plays an ever-increasing role in the design of new combustors operated with syngas fuels, as it assumes much higher values for hydrogen-rich gases compared with natural gas.

In order to describe $S_T$ for syngas mixtures and compare it with that of natural gas, insights on the effects of molecular transport have to be advanced. The significance of such effects on $S_T$ has been highlighted in the review by Lipatnikov & Chomiak (2005), concluding that in fuel-lean syngas/air turbulent combustion, molecular transport effects are still important and dominated by the $H_2$ component.

The turbulent flame speed is determined by the extent of the flame front surface area wrinkling and by the effect the flame wrinkles have on the local propagation speed of the flamelets. In any premixed flame (laminar or turbulent), the growth of an initial wrinkle is affected by the hydrodynamic Darrieus–Landau (DL) instability (Landau 1944). DL instabilities enhance the flame front wrinkling and therefore $S_T$. The effects of pressure on DL instabilities during turbulent combustion have been first reported for methane fuels by Kobayashi *et al.* (1996) and more recently for syngas mixtures by Daniele *et al.* (2011) and Ichikawa *et al.* (2011). The effect of elevated pressure on the DL flame front instability was studied analytically by Kobayashi *et al.* (1996) using the dispersion formula of Sivashinsky (1983) and more recently by Creta & Matalon (2011) who investigated theoretically the propagation of premixed flames in two-dimensional homogeneous isotropic turbulence using a Navier–Stokes/front-capturing methodology within the context of hydrodynamic theory. Nonetheless, there is still controversy regarding the precise impact of the DL instability at elevated pressures, as recently discussed by Lipatnikov & Chomiak (2010). Another important instability affecting flame front propagation characteristics in fuel-lean combustion is driven by thermal-diffusive imbalance (e.g. for fuels with Lewis numbers $Le < 1$). In particular, lean premixed hydrogen combustion is strongly affected by preferential-diffusive-thermal (PDT) effects, as summarized by Lipatnikov & Chomiak (2005).

Understanding the DL and PDT effects, as well as their coupling and their interaction with the flame stretch, is of fundamental importance for turbulent combustion. This understanding leads to a description of flame front propagation at widely disparate scales: at large scales with relevant velocity $S_T$ and at small scales with corresponding velocity the stretched laminar flame speed $S_{L,k}$.

Despite the increasing research activities in premixed syngas combustion, as discussed by Cheng (2009), there are still many open questions that call for pressing answers. In contrast to the extensive knowledge gained during the last few decades for hydrocarbons (especially $CH_4$), few experimental data are available in the literature for syngas fuels at elevated pressures and preheats (Daniele, Jansohn & Boulouchos 2009; Daniele *et al.* 2011; Ichikawa *et al.* 2011; Kobayashi *et al.* 2013). Moreover, turbulent flame speed data in the literature are generally not directly comparable, due to the different adopted definitions for $S_T$ and the different experimental methodologies used. The lack of syngas data becomes very evident especially when considering conditions relevant to gas turbines, involving elevated pressures (1–3 MPa), high preheat temperatures (600–700 K) and large turbulence intensities ($u'/S_L > 50$).

Daniele *et al.* (2009, 2011) presented, for the first time in the literature, global-consumption-based normalized turbulent flame speeds for various fuel-lean syngas/air mixtures at gas turbine relevant conditions. In the present work we further expand the analysis presented by Daniele *et al.* (2011) by adding a second methodology for determining the mean consumption turbulent flame speed and by extending the database with pure hydrogen turbulent combustion experiments.

The aim of this work is to describe the flame propagation characteristics at large and small spatial scales for syngas fuels and also for pure $H_2$, and compare them with corresponding $CH_4$ results under conditions relevant to gas turbines. A novel combination of two different approaches (global consumption and mean fractal-based consumption) is presented, and a methodology is proposed to derive the mean propagation speed of flamelets in a turbulent flow field. Normalized turbulent flame speeds are obtained by applying fractal analysis in a statistically large ensemble of flame realizations, and the results are then compared with the global consumption rate computed at the mean progress variable $\langle c \rangle = 0.50$ contour.

This article is organized as follows. The experimental methodology and measuring techniques are outlined in § 2, while data reduction analyses for the assessment of turbulent flame speeds are reported in § 3. Section 3, in particular, elaborates on fractal analysis, which is used for assessing the mean propagation speed, by presenting an improved methodology for the evaluation of the flame front fractal dimension. Finally, the main results on turbulent flame speeds, stretched laminar flame speeds, average Markstein numbers and Markstein length scales follow suit in § 4.

## 2. Experimental details

### 2.1. *High-pressure test rig*

Experiments have been performed in a high-pressure, optically accessible combustion chamber delivering a maximum thermal power of 1 MW (figure 1). The reactor chamber is cylindrical, with a length of 320 mm and an inside diameter of 75 mm. It is made of a double-wall quartz tube with cooling air flowing in the annular section (for more details, see Griebel *et al.* 2002; Daniele *et al.* 2009). A 25 mm diameter tube, coaxial to the reactor delivers the fuel/air mixture. Within this tube, fuel is injected and mixed with electrically preheated air 400 mm upstream of the combustion chamber. Fuel injection is accomplished in a co-flow configuration with the preheated

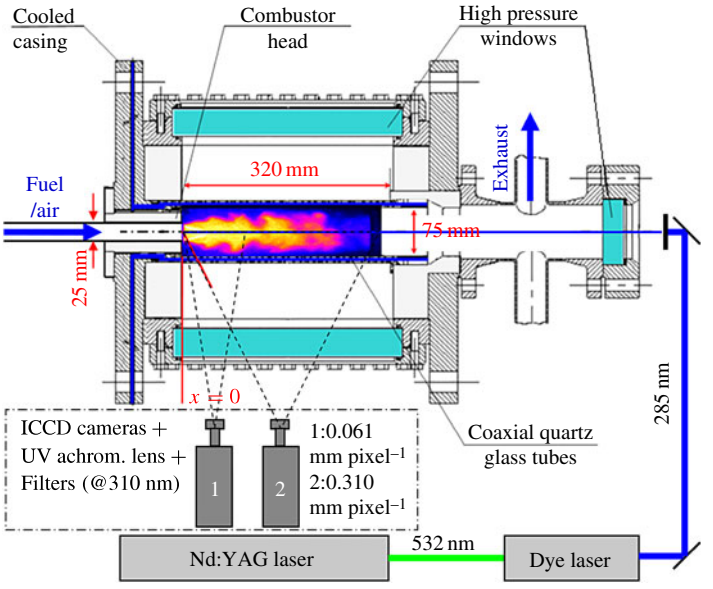


FIGURE 1. Experimental set-up: high-pressure turbulent burner and OH-PLIF optical arrangement.

air, through an array of five jets (1 mm in diameter) uniformly distributed along the periphery of the delivery tube. For the above arrangement, mixing of the two streams is considered to be perfect; this is attested by turbulent scalar mixing correlations and further verified by analysis of the resulting $NO_x$ emissions at the reactor exit. A sudden radial expansion by a factor of three between the delivery tube and the combustion chamber induces an outer toroidal recirculation zone, which stabilizes the flame. There is no swirl or piloting flame applied. Pressurization is achieved by a cylindrical steel tank enclosing the reactor and delivery tube. High-pressure air is supplied by an oil-free compressor. Optical access to the reaction zone is provided by three high-pressure quartz windows positioned on the tank, two side ones and one along the reactor axis (see figure 1).

### 2.2. *Measuring techniques*

The measurements included instantaneous turbulent flow field data, acquired with digital particle image velocimetry (PIV) and flame front imaging, achieved by means of planar laser-induced fluorescence of the OH radical (OH-PLIF).

Following the approach of earlier works (Daniele *et al.* 2009, 2011), flame speeds derived from the OH-PLIF images were correlated with local turbulence properties extracted from the PIV experiments. Such properties were the turbulence intensity ($u'$) and the integral length scale ($L_T$) at the centreline position of the flame front. Turbulence intensity was calculated from the two-dimensional PIV data as $u' = [(u^2 + 2v^2)/3]^{1/2}$, by considering the azimuthal velocity fluctuations equal to the radial fluctuations $v$; moreover, $L_T$ referred to the longitudinal integral length scale of the axial velocity component ($L_{xx}$). Centerline values of the turbulence intensity were actually representative of all flame front positions, since measurements have shown that the average flame front surface closely corresponds to a $u'$ isosurface (Siewert 2005). This is illustrated in figure 2, providing isocontours of $u'$, $L_T$ and the progress

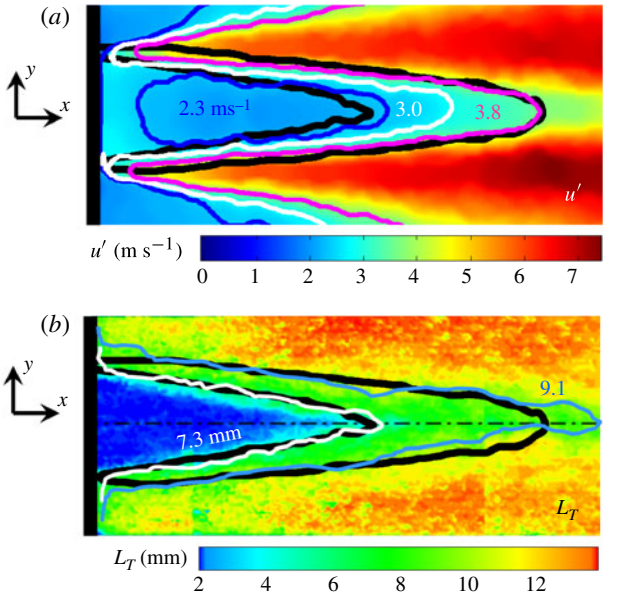


FIGURE 2. (*a*) Two-dimensional intensity map of $u'$ and three selected $u'$ isocontours: $u' = 2.3$ m s$^{-1}$ (blue line), $u' = 3.0$ m s$^{-1}$ (white line) and $u' = 3.8$ m s$^{-1}$ (purple line). (*b*) Two-dimensional intensity map of $L_T$ and two selected $L_T$ isocontours: $L_T = 7.3$ mm (white line) and $L_T = 9.2$ mm (blue line). The two black lines define the flame contour locations $\langle c \rangle = 0.05$ and $\langle c \rangle = 0.95$ for flame no. 10 in table 1. The $\langle c \rangle = 0.50$ flame contour practically overlaps with the $u' = 3.0$ m s$^{-1}$ line and therefore is not shown for clarity. The image size is 118 mm in $x$ and 50 mm in $y$.

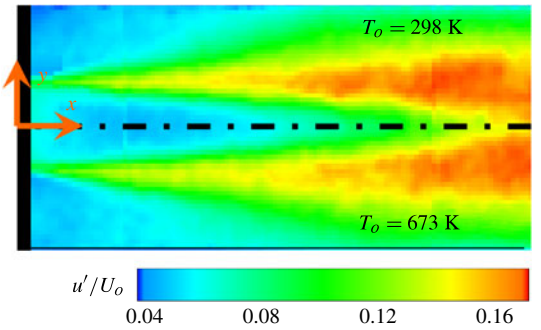


FIGURE 3. Two-dimensional intensity maps of $u'/U_o$ for two different preheats: $T_o = 298$ K (top half) and $T_o = 673$ K (bottom half). In both cases $U_o = 40$ m s$^{-1}$. The image size is 146 mm in $x$ and 70 mm in $y$.

variable $\langle c \rangle$ for typical syngas flames. Variations of $u'$ and $L_T$ along the flame contours $\langle c \rangle = 0.50$ are less than 15 %.

The choice of flame front rather than of inlet values for reference turbulence flow properties had the purpose of deriving parameters that are generally representative of the local flame/turbulence interactions, as discussed by Daniele *et al.* (2011).

The PIV database consisted of non-reacting flow measurements (acquired with a dedicated pulsed twin Nd:YAG laser system (Quantel–Brilliant), which were also used by Daniele *et al.* (2011)) and have been described in detail elsewhere (Siewert 2005). The non-reactive nature of the measurements negated thermal-gradient-induced velocity biasing. The noise-free root mean square (r.m.s.) velocity measurement error calculated from the employed optical parameters and pulse delay is estimated to 0.3 m $s^{-1}$ (a detailed discussion on PIV errors has been presented in an earlier turbulent channel-flow combustion study (Appel *et al.* 2005)).

Turbulence parameters mainly depended on the inlet velocity $U_o$ and not on mixture preheat or pressure. The effect of mixture preheat is illustrated in figure 3 providing $u'/U_o$ maps for two cases at 298 and 673 K and $U_o = 40$ m $s^{-1}$, indicating average differences of less than 10 %. The effect of pressure is investigated in an ongoing PhD thesis (Lin 2013), indicating $u'$ differences similar to those observed due to preheat. It is clarified, however, that while $u'$ and $L_T$ remain largely unaffected by pressure, the small scales of turbulence decrease as pressure increases due to the increased turbulent Reynolds numbers. The independence of $u'$ and $L_T$ on pressure has also been attested in other high-pressure turbulent combustion studies (Lachaux *et al.* 2005).

The OH-PLIF set-up is also depicted in figure 1. A pulsed Nd:YAG/dye laser system (Quantel YG981/TD90, 12 ns pulse duration) produced a beam at 284 nm having an energy of 12 mJ per pulse. The beam was converted to a light sheet by a cylindrical lens. Only the central part of the light sheet (with nearly uniform intensity) that had energy of ∼4 mJ per pulse was used in the experiments. The light sheet entered the combustor through the quartz window at the rear flange of the tank (see figure 1) and propagated in the counterflow direction. The 284 nm radiation excited the $Q_1(9)$ and $Q_2(8)$ lines of the OH A-X(1-0) transition. The fluorescence of both OH (1-1) and (0-0) transitions at 308 and 314 nm, respectively, was collected through a dielectric bandpass filter centred at 310 nm. The laser sheet thickness was estimated to be ∼0.1 mm, at least over the region imaged with camera no. 1 (see figures 1 and 4*a*).

The emitted fluorescence light was collected at a 90° angle using two intensified CCD cameras equipped with a UV achromatic lens system and appropriate dielectric filters. In contrast to our earlier works that employed a single imaging camera (Daniele *et al.* 2009, 2011), two intensified cameras were herein used for imaging different viewing areas. The first camera acquired high-resolution images for detailed analysis of the flame front corrugation at small scales, while the second camera recorded the entire flame front area for the ensuing global mass consumption analysis. The resolutions of the two cameras were 0.061 and 0.310 mm $pixel^{-1}$, respectively. The difference in the image sizes of the two cameras is depicted in figure 4(*a*,*b*) for the same flame. To ensure good statistics, 400 single-shot OH-PLIF images were collected for every investigated flame. Given the drop of the laser-induced fluorescence (LIF) signal with rising pressure and the need to maintain good quality single-shot images for the subsequent fractal analysis, we have considered in the present work flames up to 1.25 MPa (as opposed to 2.0 MPa in Daniele *et al.* (2011)).

Typical OH intensity profiles across the instantaneous flame are shown in figure 4(*c*), indicating a sharp transition between reactants and products and, hence, high quality of the ensuing flame data. A local thresholding procedure was used to delineate the flame contour, which is summarized next (for details see Daniele *et al.* 2009). The threshold was defined as 50 % of the maximum local intensity of the 400-samples-average LIF image. This procedure could effectively capture the steepest gradient of the signal intensity. The application of standard gradient-based edge-detection techniques did not yield as good results due to the large variety in the gradient

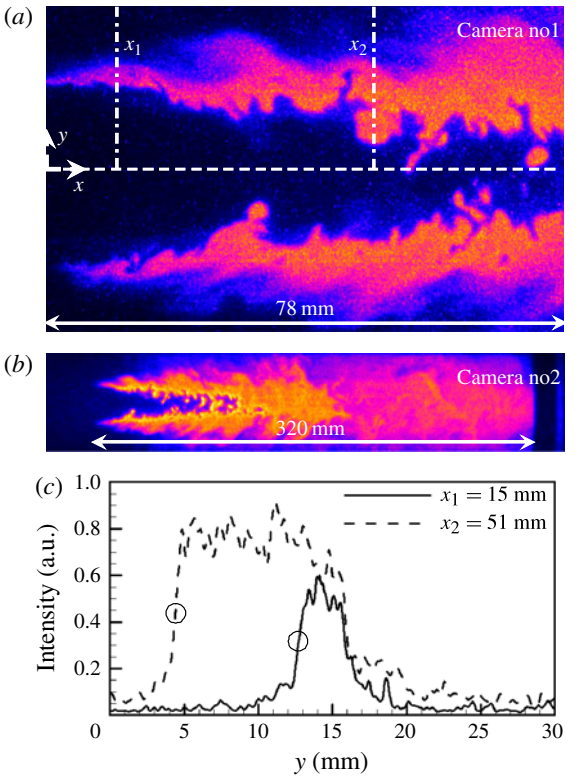


FIGURE 4. Flame imaging of the two cameras: (*a*) camera no. 1, 0.061 mm pixel$^{-1}$; (*b*) camera no. 2, 0.310 mm pixel$^{-1}$. Transverse profiles of the OH intensity are plotted in (*c*) for two locations marked $x_1$ and $x_2$ in (*a*). The two circles in (*c*) define the instantaneous flame front location computed by the employed thresholding technique.

distribution of the LIF images. Application of the adopted thresholding procedure is shown in figure 4(*c*), whereby the two circles indicate the computed location of the instantaneous flame front at two selected positions. Sensitivity analysis indicated that the precise threshold value did not affect the evaluated instantaneous flame properties (i.e. fractal dimensions).

For the high-resolution camera no. 1, the modulation transfer function (MTF) at the photocathode plane of the 25 mm image intensifier was 34 line pairs per millimetre. This corresponded to approximately 0.1 mm in the observation plane and to about 2 pixels at the detector chip plane. The latter size provided enough oversampling and Kell factor to avoid aliasing artifacts. The flame front was tracked using the steep (steepest) increase in OH intensity and no attempt was made to deduce the flame thickness. Information below 0.3 mm has been purposely disregarded in the ensuing fractal analysis, given the 0.1 mm laser sheet thickness. Amplifier noise due to photon shot noise in conjunction with the binomial distribution of the quantum efficiency of the photocathode, resulted in single photoelectron events with a size of approximately 0.2 mm in the observation plane. Such sizes were therefore below the set cut-off limit of 0.3 mm, rendering additional filtering dispensable.

It is finally noted that direct numerical simulation (DNS) studies have shown OH to be a good marker for the flame front in lean $H_2$ turbulent premixed combustion.

| No | $H_2$ % | CO % | $CH_4$ % | $N_2$ % | $P$ MPa | $\phi$ – | $\delta_L$ mm | $S_{L,O}$ m s$^{-1}$ | $S_{L,k}$ m s$^{-1}$ | $S_T^{0.50}$ m s$^{-1}$ | $D_2$ – | $\varepsilon_0$ mm | $u'$ m s$^{-1}$ | $L_T$ mm | $f_{BT}$ mm | $l_M$ mm | $\overline{Ma}$ – | $Le^*$ – | Colour coding |
|---|---|---|---|---|---|---|---|---|---|---|---|---|---|---|---|---|---|---|---|
| 1 | 0 | 0 | 100 | 0 | 0.25 | 0.62 | 0.25 | 0.52 | 0.47 | 1.43 | 1.29 | 10.83 | 6.42 | 8.42 | 94.24 | 0.00 | 0.01 | 0.96 | Orange |
| 2 | 0 | 0 | 100 | 0 | 0.25 | 0.71 | 0.21 | 0.69 | 0.67 | 2.08 | 1.31 | 10.21 | 5.61 | 7.63 | 59.52 | 0.00 | 0.01 | 0.96 | |
| 3 | 20 | 20 | 60 | 0 | 0.25 | 0.62 | 0.22 | 0.66 | 1.01 | 2.69 | 1.29 | 9.25 | 4.32 | 6.54 | 54.56 | –0.04 | –0.17 | 0.92 | Black |
| 4 | 10 | 10 | 60 | 20 | 0.25 | 0.62 | 0.24 | 0.56 | 0.64 | 1.93 | 1.30 | 10.69 | 5.54 | 7.56 | 78.12 | –0.01 | –0.03 | 0.94 | Grey |
| 5 | 33 | 67 | 0 | 0 | 0.10 | 0.40 | 0.76 | 0.77 | 1.85 | 3.53 | 1.23 | 11.36 | 3.36 | 5.30 | 43.40 | –0.25 | –0.33 | 0.93 | |
| 6 | 33 | 67 | 0 | 0 | 0.25 | 0.41 | 0.33 | 0.54 | 0.93 | 2.50 | 1.28 | 9.79 | 5.10 | 7.15 | 54.56 | –0.04 | –0.11 | 0.93 | Green |
| 7 | 33 | 67 | 0 | 0 | 0.50 | 0.38 | 0.22 | 0.30 | 0.93 | 2.93 | 1.30 | 9.43 | 4.09 | 6.32 | 50.84 | –0.05 | –0.24 | 0.93 | |
| 8 | 50 | 50 | 0 | 0 | 0.10 | 0.38 | 0.71 | 0.89 | 2.35 | 4.28 | 1.23 | 10.39 | 3.11 | 4.55 | 43.40 | –0.35 | –0.50 | 0.78 | |
| 9 | 50 | 50 | 0 | 0 | 0.10 | 0.41 | 0.67 | 1.10 | 2.50 | 4.56 | 1.22 | 11.31 | 2.98 | 3.86 | 42.16 | –0.34 | –0.50 | 0.78 | |
| 10 | 50 | 50 | 0 | 0 | 0.10 | 0.44 | 0.65 | 1.31 | 2.66 | 4.88 | 1.21 | 12.48 | 2.98 | 3.86 | 37.20 | –0.33 | –0.50 | 0.78 | |
| 11 | 50 | 50 | 0 | 0 | 0.25 | 0.38 | 0.31 | 0.54 | 1.33 | 3.26 | 1.28 | 8.58 | 3.51 | 5.59 | 50.84 | –0.11 | –0.36 | 0.78 | Red |
| 12 | 50 | 50 | 0 | 0 | 0.50 | 0.38 | 0.19 | 0.35 | 1.35 | 3.96 | 1.29 | 9.01 | 3.32 | 5.20 | 34.72 | –0.11 | –0.55 | 0.78 | |
| 13 | 50 | 50 | 0 | 0 | 1.00 | 0.38 | 0.15 | 0.19 | 1.30 | 4.29 | 1.27 | 10.35 | 3.15 | 4.70 | 37.20 | –0.08 | –0.57 | 0.78 | |
| 14 | 50 | 50 | 0 | 0 | 1.25 | 0.42 | 0.11 | 0.22 | 1.44 | 5.11 | 1.29 | 8.27 | 3.01 | 4.02 | 28.52 | –0.08 | –0.76 | 0.78 | |
| 15 | 67 | 33 | 0 | 0 | 0.25 | 0.38 | 0.27 | 0.64 | 1.54 | 3.79 | 1.28 | 9.56 | 3.41 | 5.40 | 34.72 | –0.13 | –0.49 | 0.62 | Blue |
| 16 | 70 | 0 | 0 | 30 | 0.25 | 0.35 | 0.18 | 0.55 | 2.69 | 5.73 | 1.23 | 10.97 | 2.99 | 3.92 | 19.84 | –0.34 | –1.86 | 0.29 | Light |
| 17 | 70 | 0 | 0 | 30 | 0.50 | 0.36 | 0.20 | 0.26 | 2.23 | 5.66 | 1.26 | 8.49 | 2.96 | 3.76 | 22.32 | –0.22 | –1.08 | 0.29 | blue |

TABLE 1. Representative subset of experimental conditions ($T_o = 623$ K, $U_o = 40$ m s$^{-1}$). The provided composition of the fuel stream is percentage by volume.

For lean $H_2$ mixtures ($\varphi < 0.5$) Baum *et al.* (1994) reported that the OH radical is concentrated in the reaction zone and only at considerably higher equivalence ratios and much higher flame temperatures (∼2800 K) may the peak OH occur behind the peak heat-release zone. Similar results have also been reported by Bell *et al.* (2007).

### 2.3. *Test matrix*

The investigated fuel mixtures varied from pure $CH_4$ to pure $H_2$ (the latter diluted with $N_2$), including mixtures with different $H_2$–CO compositions, and two cases whereby $CH_4$ was cofired with syngas. These fuel mixtures were representative of different scenarios relevant to IGCC power plants, accounting for different feedstocks and various gasification processes. The strategy of the fuel mixtures selection has been detailed by Daniele *et al.* (2009).

The experimental database comprises 53 different flames. A representative subset of the investigated flames is shown in table 1, where the volumetric composition of the fuel stream and the operating conditions are provided, along with other measured and/or derived turbulent and combustion parameters (the effective Lewis numbers of the mixture, $Le^*$, are calculated according to Law, Jomaas & Bechtold (2005)). All measurements are performed at a preheat temperature $T_o = 623$ K and an inlet velocity $U_o = 40$ m s$^{-1}$. The pressure ranged from 0.10 to 1.25 MPa and the equivalence ratio from 0.3 to 0.7. Table 1 is colour-coded to easily differentiate the various fuel mixtures in the forthcoming discussion of the results. This test matrix is relevant to gas turbine applications and all investigated conditions are further positioned in figure 5 on the Borghi diagram as modified by Peters (1999) Most of the data points fall into the 'thin reaction zones' regime of turbulent combustion, although recent experiments in Yuen & Gülder (2013) suggest a narrower range for flamelet applicability. Finally, turbulence in practical combustors is high enough such that

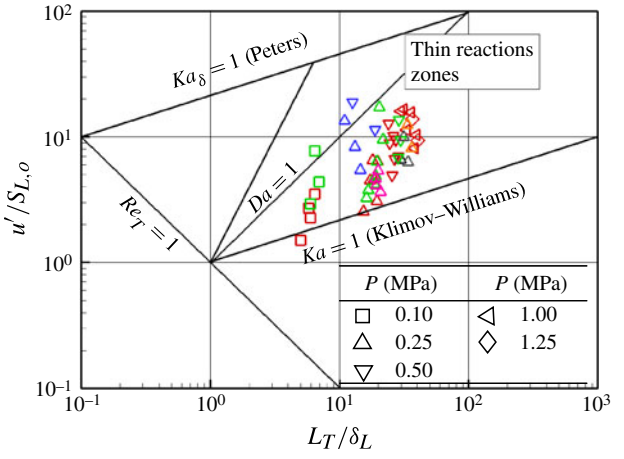


FIGURE 5. Experimental conditions on the Borghi–Peters diagram. Colour coding of symbols according to composition, as in table 1.

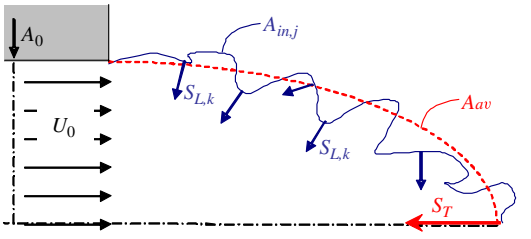


FIGURE 6. Schematic of the different areas across the flame: $A_{in,j}$ is the instantaneous flame front area of the $j$th realization and $A_{av}$ the average flame front area.

energy cascade concepts and Kolmogorov spectra are valid (Petersen & Ghandhi 2009).

## 3. Data reduction

The applied methodologies are clarified with the schematic in figure 6, depicting the inlet section and the flame front (due to axisymmetry, only half of the domain is shown). Flame speeds were evaluated by applying continuity analysis and considering that mass throughput is conserved through the following three surfaces in figure 6: inlet section ($A_o$), the average flame front surface ($A_{av}$) and the ensemble average of all corrugated instantaneous flame front surfaces ($A_{in}$).

The mass balance

$$\rho_o A_o U_o = \rho_o A_{av} S_T \tag{3.1}$$

is recast to

$$S_T = \frac{A_o}{A_{av}} U_o \tag{3.2}$$

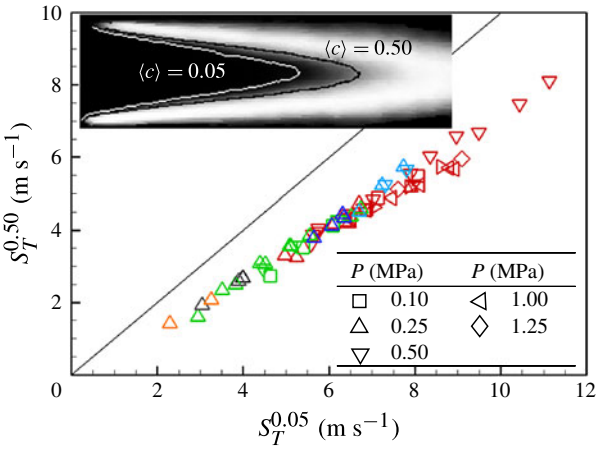


FIGURE 7. Dependence of $S_T$ on the progress variable $\langle c\rangle$. Colour coding of symbols according to composition, as in table 1.

to derive absolute values for $S_T$, while the ensemble average in

$$\frac{S_T}{S_{L,k}} = \overline{\left(\frac{A_{in,j}}{A_{o,j}}\right)} \tag{3.3}$$

yields normalized flame speeds $S_T/S_{L,k}$. These two quantities will be elaborated upon in the results section. The overbar in (3.3) denotes ensemble averaging over 400 flame samples ($j = 1$–$400$), $A_{in,j}$ the instantaneous corrugated flame area of the $j$th realization and $A_{o,j}$ the instantaneous smoothened flame area of the $j$th realization, measured with an appropriately large yardstick (see § 3.2).

### 3.1. *Turbulent flame speed: global consumption*

To evaluate $S_T$ from (3.2), $A_o$ and $U_o$ are known from the geometry and the inlet conditions, while the average surface $A_{av}$ is derived from 400 single-shot realizations of camera no. 2 (figure 4*b*). The average area $A_{av}$ is evaluated with a progress variable approach, as described by Daniele *et al.* (2009, 2011). Daniele *et al.* (2011) reported turbulent flame speeds associated with the $\langle c\rangle = 0.05$ progress variable contour based on the measured OH radical, which was representative of the faster propagating flame fronts in the turbulent brush thickness. Within this work, contours of $\langle c\rangle = 0.50$ are predominantly used. This choice is driven by the need to compare results obtained with (3.2) and (3.3), as will be clarified in the forthcoming § 4.2. In figure 7 the two progress variable contours are drawn on an averaged OH-PLIF sample image and the correlation between the two calculated $S_T$ (referred to as $S_T^{0.05}$ and $S_T^{0.50}$) for a data subset is also given; evidently, $\langle c\rangle = 0.05$ corresponds to smaller flame areas and, hence, to higher flame speeds $S_T^{0.05}$.

Turbulent flame speeds evaluated with the methodology of (3.2) are understood as global consumption per unit time.

### 3.2. *$S_T/S_{L,k}$-normalized fractal-based mean consumption*

The ratio $A_{in,j}/A_{o,j}$ in (3.3) is derived from the high-resolution camera no. 1 (figure 4*a*) by analysing every single image of the 400 instantaneous OH-PLIF realizations on half the flame domain (i.e. upper half in figure 4*a*). The evaluation involves fractal analysis

for each instantaneous flame realization $j$ according to (Gouldin, Bray & Chen 1989)

$$\frac{A_{in,j}}{A_{o,j}} = \left(\frac{\varepsilon_o}{\varepsilon_i}\right)^{D_2-1}, \tag{3.4}$$

where $\varepsilon_i$, $\varepsilon_o$ and $D_2$ denote the inner cutoff, outer cutoff and two-dimensional fractal dimension of each analysed instantaneous flame contour, respectively. The extraction of the fractal parameters is elaborated on in the next section. Normalized turbulent flame speeds $S_T/S_L$ evaluated from (3.3) and (3.4) provide the normalized mean consumption per unit time. The combination of (3.2) and (3.3) yields the magnitude of $S_{L,k}$ which is understood as the mean propagation velocity of the flamelets. This parameter contains information on the interaction between stretch and PDT effects and it is derived with this combined approach for the first time. The flame speed $S_{L,k}$ is to be distinguished from the unstretched laminar flame speed, $S_{L,o}$, which has been used by Daniele *et al.* (2011) and was computed using the one-dimensional freely propagating laminar flame package Cantera (Cantera 1998) with the GRI-3.0 chemical reaction mechanism (Smith *et al.* 2000). It is noted, however, that accurate laminar flame properties for syngas and hydrogen present a challenge, since validated reaction mechanisms at elevated pressures and preheats for such fuels are still lacking (Natarajan, Lieuwen & Seitzman 2007). Nonetheless, comparisons between GRI-3.0 and a recently developed mechanism for syngas and hydrogen (Li *et al.* 2007) yielded, for the fuel compositions in table 1, $S_{L,o}$ differences of up to 18 % at 0.1 MPa and twice as high for 1.0 MPa. However, even if such differences reflected deviations from the true $S_{L,o}$, they would not affect the ensuing discussion of the results.

Estimated values of $S_{L,k}$ in laminar and turbulent flames have been reported for hydrocarbons and for $H_2$ fuels, for example by Metghalchi & Keck (1980), Gu *et al.* (2000), Kwon & Faeth (2001), Lamoureux, Djebaili-Chaumeix & Paillard (2003), Huang *et al.* (2006), Bradley *et al.* (2007), Weiss, Zarzalis & Suntz (2008) and Chen (2011), by performing experiments in constant volume chambers or internal combustion (IC) engines. In this work $S_{L,k}$ is derived from stationary combustion experiments under gas-turbine-like conditions.

3.2.1. *Calculation of fractal parameters: methodologies*

Given the importance of $D_2$ for the subsequent assessment of $S_{L,k}$, different literature approaches for evaluating the fractal dimension $D_2$ are presented below and a new methodology is further proposed. Two approaches for the evaluation of the fractal parameters have been considered, the 'box counting' (BC) and the 'stepping caliper' (SC) (Mandelbrot 1985) methods. These methodologies have already been used in other works for the assessment of normalized turbulent flame speeds and have also been compared against each other (see Mantzaras, Felton & Bracco 1989; Takeno, Murayama & Tanida 1990; Shepherd, Cheng & Talbot 1992; Chen & Mansour 1999; Gulder *et al.* 2000; Cohe *et al.* 2007). Both methodologies are based on the concept of measuring the length of a curve (embedded in a two-dimensional space) with geometric yardsticks of different scales. For a series of scales $i = 1$–$n$:

(i) the BC method counts the number $n_i$ of adjacent square boxes with side length $r_i$ that are required to cover the curve length;

(ii) the SC method measures how many $n_i$ consecutive segments (calipers) having length $r_i$ are contained within the curve.

If the analysed curve has a fractal nature, a power law dependence $n_i \sim r_i^{-D_2}$ is recovered.

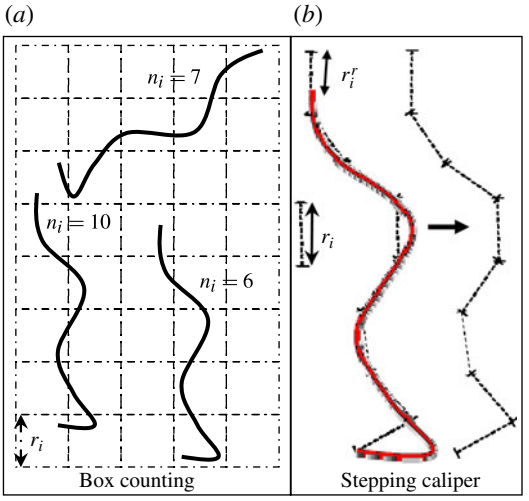


FIGURE 8. Large-scale error for BC and SC methodologies applied to the same curve: (*a*) BC algorithm for the same curve at three different orientations; (*b*) SC algorithm.

In most fractal shapes, the range over which the curve exhibits fractal behaviour is limited by the inner and outer cutoff scales ($\varepsilon_i$ and $\varepsilon_o$, respectively); outside this range the exponent of the aforementioned power law becomes $-1$, as any box or caliper smaller/larger than $\varepsilon_i/\varepsilon_o$ cannot reveal additional corrugations.

The greatest difficulty arising with the BC method is that many values of $n_i$ may correspond to a given scale $r_i$, depending on the topology of the analysed curve and on the scale itself (Foroutan-pour, Dutilleul & Smith 1999; Soille & Rivest 1996). This is illustrated in figure 8(*a*), whereby for the same curve three different values of $n_i$ are obtained for three different curve orientations.

The SC method also leads to intrinsic errors, the main one being that for most of the considered calipers $r_i$, the analysed curve will not contain an integer number of them. Accounting for the remaining 'last caliper' (not entirely contained within the curve) leads to an overestimation of the length, while the correct length is $(n_i r_i – r_i^r)$, where $r_i^r$ represents the fraction of caliper which falls outside the curve. This is illustrated in figure 8(*b*) and will be discussed in more detail next.

In summary, key differences between the BC and SC methodologies when analysing an ideal fractal curve are: (*a*) for the BC, no set of boxes with size $r_i$ exist, yielding the exact fractal dimension; and (*b*) for the SC, there always exists a series of scales $r_i$ (custom-defined), which count integer numbers of caliper $n_i$ ($r_i^r = 0$) and thus yield the exact fractal dimension.

For this reason, and because high accuracy is required in the flame front analysis due to the small variation of $D_2$ in turbulent flames, the SC method has been selected for calculating the normalized turbulent flame speeds. This method is further described in the next section wherein an improved algorithm for calculating $D_2$ is proposed. Consequently, results obtained with the BC method will be shown just for comparison.

3.2.2. *Stepping caliper method: errors and proposed new algorithm*

When the last caliper falls off the curve, an error is introduced since only a fraction of it is contained within the curve (figure 8*b*). This leads to an overestimation of

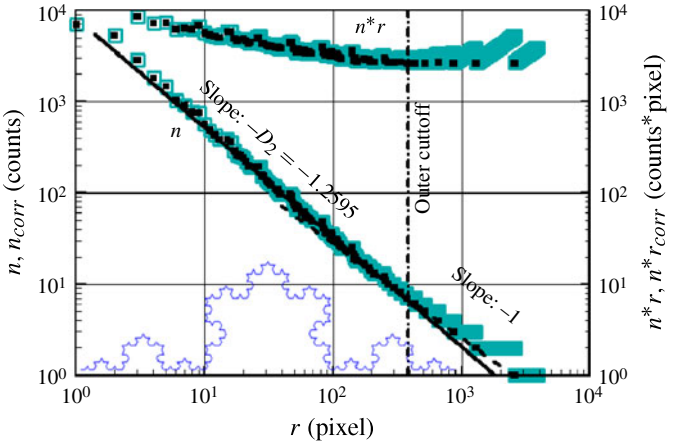


FIGURE 9. Correction for the large-scale error demonstrated for the von Koch curve (see the inset curve). Selected pairs of correct counts ($n_{corr}$) are denoted by black symbols. Grey symbols (shown in green online) correspond to all possible combinations of $n$–$r$.

$n_i$, when this caliper is accounted for, or to an underestimation of $n_i$ when the last caliper is not considered. This problem was already highlighted by Chen & Mansour (1999), who proposed a correction that is discussed later in this section. It is therefore demonstrated that, when analysing a general curve, any arbitrary choice of caliper lengths will not provide the correct result. Moreover, for a general curve such as a flame front a 'proper' set of calipers is not *a priori* known.

The importance of the large-scale error is demonstrated in figure 9, presenting plots of $n$ versus $r$ (lower line, referring to the left ordinate axis) and plots of $r \cdot n$ versus $r$ (upper line, referring to the right ordinate axis) for a curve composed of six sequential von Koch snowflakes (constructed with five recursions) arranged in a row (see the inset to figure 9 for the shape of a single von Koch element), which has a known fractal dimension $D_2 = 1.2619$. For the von Koch curve in figure 9, the exact $\varepsilon_i$ is not constant due to the digitalization of the image and assumes values $\varepsilon_i = 5$–$6$ pixels. Therefore, the calculated $\varepsilon_o$ is $\varepsilon_o = 3^4\varepsilon_i = 405$–$486$ pixels, while the exact one is 434 pixels (start-to-end length of a single von Koch element). The square symbols ($n$ versus $r$, shown in green online) in figure 9 are representative of the counts of all calipers ($r = 1$–$4000$, which is a value 1.5 times larger than $6\varepsilon_o$) exemplifying the importance of the error discussed before.

In the same figure, the filled black square symbols ($n_{corr}$ versus $r$) are indicative of what is left out after rejecting all caliper lengths yielding the same value of $n$, except for the shortest length caliper. This procedure was followed based on the consideration that when the curve is perfectly matched by $n_k$ calipers of size $r_k$, the calipers having size $r_{k+l}$ will fall off the curve, producing the mentioned error. From this point on, all of the caliper sizes will count the same $n_{k+1}$ until a perfect match is realized again. The correction of the error is then possible by removing those false pairs $n_i$–$r_i$ for $i > k$. Following this procedure, an estimated fractal dimension of 1.2595 is obtained, which excellently matches the theoretical value. It is subsequently demonstrated that to eliminate such an error, knowledge of all pairs $n_i$–$r_i$ is necessary.

The curve $r \cdot n$ versus $r$ in figure 9 has the property of a zero slope outside the fractal range. This characteristic property has been used to determine $\varepsilon_o$. Once $\varepsilon_o$ is

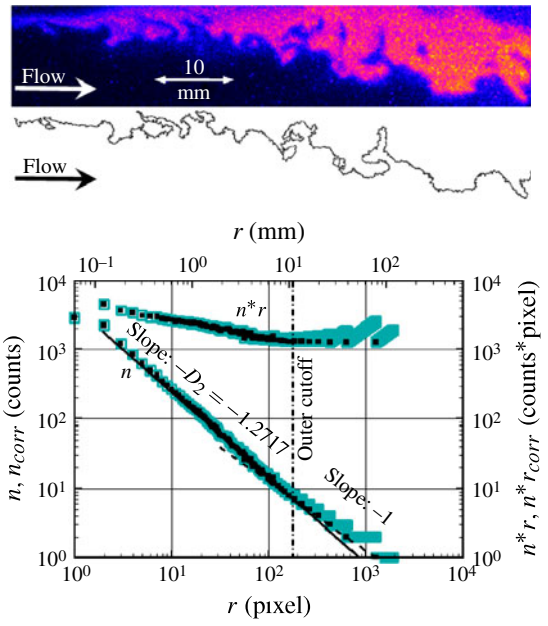


FIGURE 10. Correction for the large-scale error demonstrated for a syngas flame. Instantaneous OH-PLIF image and extracted flame front are also shown ($H_2$–CO/50–50, $P = 0.10$ MPa, $T_o = 623$ K, $U_o = 40$ m s$^{-1}$, $\Phi = 0.44$, flame no. 10 in table 1). Notation as in figure 9.

determined, the calculated slope of the lower curve in figure 9 for $r_i \geqslant \varepsilon_o$ is $-1.0044$, which matches well the theoretical slope of $-1.0$ for this non-fractal part of the curve. As the presented curve is a series of 6 snowflakes and each snowflake is 434 pixels long, this value represents $\varepsilon_o$. The calculated value is 375, which is a conservative estimate of the true $\varepsilon_o$. From the comparison between black and grey (green online) symbols in figure 9 it becomes clear that an arbitrary choice of the caliper set can falsify the correct values of $\varepsilon_o$ and $D_2$.

Without applying the correction, by analysing the grey (green online) symbols in figure 9, the extraction of the outer cutoff is highly inaccurate if not impossible; consequently, the extraction of the fractal dimension is compromised. In this case, the estimated fractal dimension (using least-square linear fit) is 1.0065 when no outer cutoff is considered, and it assumes a value of 1.24 when using the outer cutoff computed with the above-described improved methodology (in normal cases, $\varepsilon_o$ would remain unknown).

The application of the SC methodology corrected for the large-scales error is shown for a flame front ($H_2$–CO/50–50, $P = 0.10$ MPa, $T_o = 623$ K, $U_o = 40$ m s$^{-1}$, $\Phi = 0.44$, flame no. 10 in table 1) in figure 10. This figure is constructed in the same fashion as figure 9. The comparison of the two diagrams in figures 9 and 10 reveals that the considerations discussed before for the von Koch curve are also valid for the actual flame fronts.

To overcome the large-scale error, Chen & Mansour (1999) proposed to estimate the remaining part of the curve (i.e. $r_i$–$r_i^r$ in figure 8*b*) by measuring it with a caliper of 1 pixel size and then rescale the result to the actual caliper size by invoking self-similarity. However, corrections based on self-similarity are not warranted when

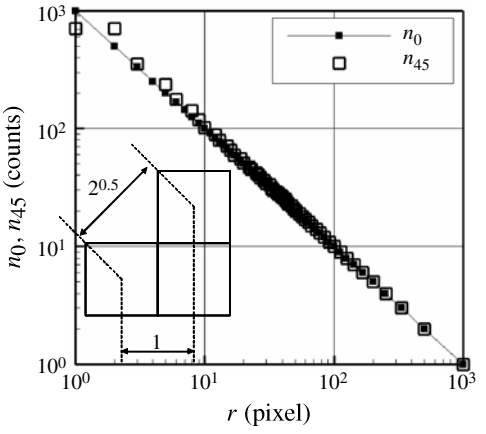


FIGURE 11. Small-scale error analyzed for a straight line either horizontal ($n_o$) or at an angle of 45° ($n_{45}$).

the remaining length is shorter than the inner cutoff scale. In the present work we did not use this correction mainly because, by relying on measurements at very small scales, a digitalization error may also appear; this is termed 'small-scale error' and is discussed at the end of this section.

For the particular case of inner cutoffs of the order of 5–6 pixels, as in the example of figure 9 (series of 6 von Koch curves), the correction of Chen & Mansour (1999) yielded a fractal dimension of 1.2532 (underestimating the correct value by ∼1 %). The comparison of our methodology with that of Chen & Mansour (1999) indicates that both procedures are able to recover the correct fractal dimension of calibration curves. Moreover, when applied to flame fronts (such as that in figure 10, whereby the inner cutoff is again ∼5 pixels long) it can be shown that the resulting differences between the two methods are again very small (∼1 %). The main distinction in the two procedures is the spread of the counts $n$ (from the fitted straight line slope) in the $n$–$r$ diagram, which is significantly smaller in our case, as depicted in figure 10 and when compared with the diagrams in Chen & Mansour (1999). For example, the standard deviation for $n$ is on average 0.2 for our methodology and 1.4 for the methodology of Chen & Mansour (1999), for both calibration curves and flame fronts. This behaviour may also affect the correct evaluation of the fractal dimension if a smaller range of calipers $r_i$ is used for this purpose.

The SC method is also affected by an error at small scales, which is especially significant for the calculation of the inner cutoff scales. To discuss this error, it is useful to first analyse a straight-line segment ($D_2 = 1$). In figure 11 the filled symbols ($n_o$ versus $r$) correspond to the segment oriented horizontally and the open symbols ($n_{45}$ versus $r$) feature the same segment inclined at 45°. In the latter case, data corresponding to the smallest calipers ($r = 1$–$10$) show a large scatter. This scatter is indicative of the error committed when assigning the value of 1 to the distance between 2 pixels regardless of how these 2 pixels are connected to each other. The maximum error is $2^{0.5} - 1$, as shown in the inset (where the three drawn squares are representative of three adjacent pixels) and has a non-negligible impact for $r < 10$ pixels. Therefore, when extracting inner cutoff scales either this error has to be corrected for, or the inner cutoff scale needs to be at least 10 pixels large. The

| No. | Curve | $D_2^{ex}$ | $D_2$ | $D_{2,r>\varepsilon_o}^{ex}$ | $D_{2,r>\varepsilon_o}$ |
|---|---|---|---|---|---|
| 1 | Snowflake von Koch (five iterations) | $\log(4)/\log(3) = 1.2619$ | 1.2595 | 1 | 1.0044 |
| 2 | Snowflake von Koch (eight iterations) | $\log(4)/\log(3) = 1.2619$ | 1.2633 | 1 | 1.0043 |
| 3 | Quadratic von Koch curve | $\log(8)/\log(4) = 1.5000$ | 1.5003 | | |

TABLE 2. Validation of the fractal analysis routine.

scatter below 10 pixels is also one of the reasons why corrections according to Chen & Mansour (1999) were not applied.

It is clarified that the aim of this work is not to extract inner cutoff scales (which are after all not readily resolvable with the 0.1 mm laser sheet thickness), but rather to give a full description of the potential inaccuracies of the SC methodology.

3.2.3. *Validation*

The routine with correction for the large-scale error was validated against the three curves listed in table 2. Therein, the exact fractal dimension, $D_2^{ex}$, and the calculated one, $D_2$, are listed for every analysed curve. Moreover, when possible, $D_{2,r>\varepsilon o}$ (for scales which are bigger than the outer cutoff) has been extracted and compared with the exact slope of $-1$ ($D_2 = 1$), to further demonstrate the precision of the methodology. Test cases no. 1 and no. 2 are representative of two von Koch snowflake curves with two different levels of construction iterations, while case no. 3 is representative of a quadratic von Koch curve. Comparison of the results shows very good agreement. The validation of the routine against different curves is mandatory, since we have experienced that it may be possible to tune a not-so-precise methodology on a single calibration curve and recover the exact result. The validation against different curves rules out the possibility of 'tuning mistakes' and ensures the best achievable result in practical curves such as flame fronts.

Validation of the method on flame front curves is not possible, since no theoretical solution for the fractal parameters is available. However, an indication of the accuracy can be obtained by extracting $D_{2,r>\varepsilon o}$. This value should be 1 if the flame front does not have a fractal nature for this scale range. The typical result provided by our routine is $1.0139 \pm 0.0080$ over 400 instantaneous flame front samples, corresponding to the particular case in figure 10 (flame no. 10 in table 1).

## 4. Results

### 4.1. *Global consumption speeds and flame surface densities*

A comparison of normalized global consumption turbulent flame speeds with literature correlations is shown in figure 12 for various fuel mixtures and pressures. In the measurements, normalization is carried out with respect to the unstretched laminar flame speed $S_{L,o}$. For the diffusionally neutral $CH_4$ fuel, the formula from Yakhot (1988) provides the best agreement with the measurements. For the various syngas fuels, the provided correlations encompass most of the data. It will be shown in § 4.6 that the observed scatter of the syngas measurements is largely due to normalization of the turbulent flame speed with the unstrained laminar flame speed.

Finally, flame surface densities (FSDs) have also been calculated. Even though the present flame analysis is based on concepts other than FSD, the FSD data are

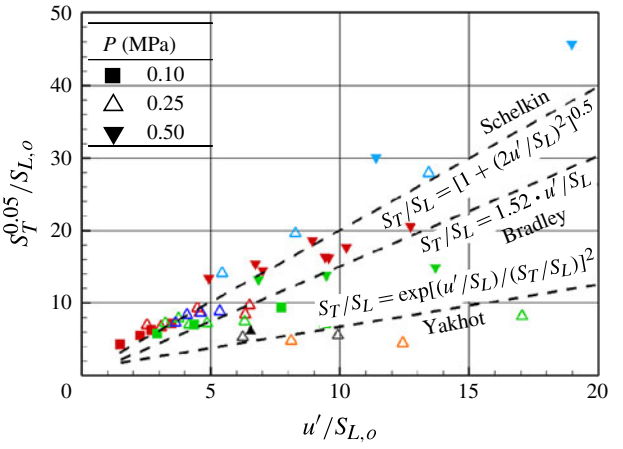


FIGURE 12. Normalized turbulent flame speed data and comparison with literature correlations from Schelkin (1943), Yakhot (1988) and Bradley (1992). Colour coding of symbols according to composition, as in table 1.

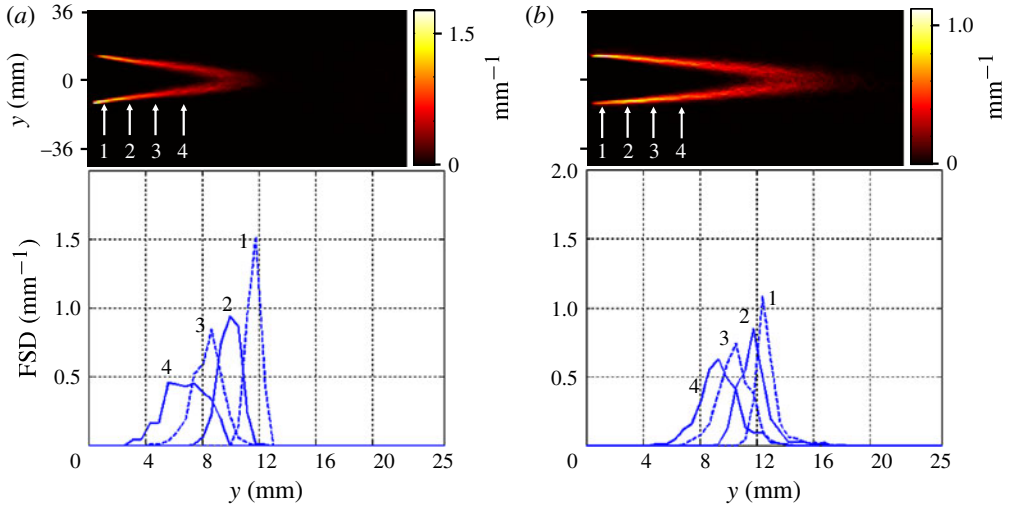


FIGURE 13. FSD two-dimensional maps for (*a*) flame no. 16 and (*b*) flame no. 6 in table 1. Transverse ($y$) plots over half the flame domain are also shown for each case at four selected axial positions $x = 9$, 22, 34 and 47 mm, marked (1)–(4).

of interest in premixed turbulent combustion modelling (such as the DNS study of Chakraborty & Cant (2011), which assessed the impact of Lewis number on the FSD transport). FSD results are plotted in figure 13 for two cases in table 1. The two-dimensional shapes and the range of values for FSDs are similar to those reported by Ichikawa *et al.* (2011).

### 4.2. *Fractal parameters*

The procedure followed for extracting fractal parameters is described next. Concerning the inner cutoff, initially the Gibson ($=L_T\,[S_{L,o}/u']^3$) and Kolmogorov scales were calculated. The Gibson scales, apart from a few cases at atmospheric pressure, resulted

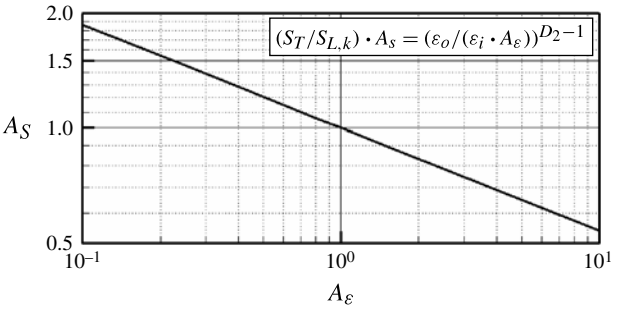


FIGURE 14. Sensitivity analysis: effect of the inner cutoff $\varepsilon_i$ on $S_T/S_{L,k}$ (for a given change of $\varepsilon_i$ by a factor of $A_\varepsilon$, the resulting factor $A_s$ for $S_T/S_{L,k}$ is plotted).

in values always smaller than the Kolmogorov scales ($\eta$) and were thus not considered. In this work we presumed that the inner cutoff scale was an order of magnitude larger than $\eta$, $\varepsilon_i = 10\eta$. An order of magnitude difference between $\eta$ and $\varepsilon_i$ has also been reported in a number of studies (Takeno *et al.* 1990; Gulder & Smallwood 1995; Kobayashi & Kawazoe 2000). It was therein suggested that inner cutoff scales are generally an order of magnitude larger than the Kolmogorov scales and of the same order of magnitude as the Taylor scales and the laminar flame thicknesses. This choice corresponds to $\varepsilon_i/\delta_L = 10Ka^{-2}$ (using the $\eta = Re_T^{-3/4}L_T$ relation for isotropic turbulence, $\nu = S_{L,o}\delta_L$, $Ka = (u'/S_{L,o})^{-3/4}(L_T/\delta_L)^{1/4}$), which closely matches the best fit of the experimental data reviewed by Gulder & Smallwood (1995).

To assess the quality of the results derived with the aforementioned assumption on $\varepsilon_i$, a sensitivity analysis has been carried out in figure 14, showing the change in $S_T/S_{L,k}$ with $\varepsilon_o$. This is illustrated in terms of the multiplicative factors $A_s$ and $A_\varepsilon$ defined according to the expression in the figure inset. The analysis was performed by considering $D_2 = 1.27$ and $\varepsilon_o = 10.3$ mm (average values over the full set of experiments presented in the paper). The plot in figure 14 indicates that a modest variation of the inner cutoff scale around its nominal value $\varepsilon_i = 10\eta$, produces a considerably smaller change in $S_T/S_{L,k}$: for example, for a factor of two error in $S_T/S_{L,k}$ the inner cutoff scale has to be off by more than one order of magnitude, while for $\pm 10\,\%$ error in $S_T/S_{L,k}$ the change in $\varepsilon_i$ must be $-30$ and $+50\,\%$, respectively.

Outer cutoff scales are extracted from the $r_i \cdot n_i$ versus $r_i$ plots for every single-shot flame image, according to the von Koch snowflake procedure shown in figure 9. In figure 15, the measured integral length scales $L_T$ (Daniele *et al.* 2011), Kolmogorov scales $\eta$ (derived as $L_T \cdot Re_L^{-3/4}$) laminar flame thicknesses (calculated from one-dimensional freely propagating flame computations using GRI-3.0 (Smith *et al.* 2000)) and the thermal thickness definition according to Poinsot & Veynante (2005) and outer cutoff scales $\varepsilon_o$ are reported for a constant pressure of 0.25 MPa and for the different investigated fuels. The $\varepsilon_o/L_T$ ratio is about two for high $u'/S_{L,o}$ ($>10$) and becomes larger at smaller $u'/S_{L,o}$.

The values of $\eta$ in figure 15 (shown instead of the inner cutoff) suggest that $\varepsilon_i = 10\eta$ is of the same order of magnitude as the laminar flame thickness (and the not-shown Taylor scale).

The fractal dimension $D_2$ has been extracted for every measured condition from the slope in the $n_i$ versus $r_i$ plot, for the 400 single-shot realizations (as depicted for one sample in figure 10) and then averaged over the 400 samples. Fractal dimensions for

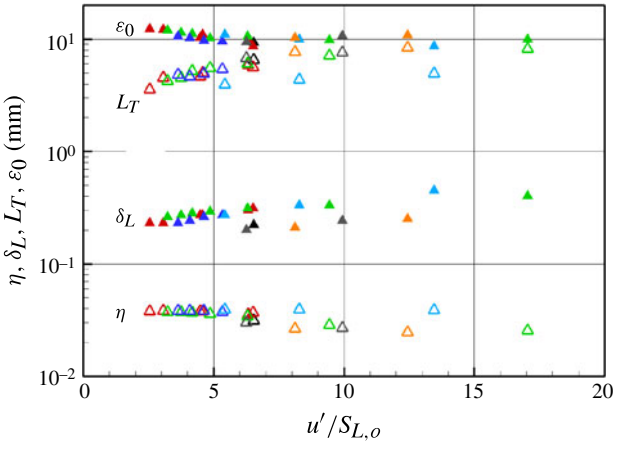


FIGURE 15. Variation of $\eta$, $\delta_L$, $L_T$ and $\varepsilon_o$ versus $u'/S_{L,o}$ ($P = 0.25$ MPa). Colour-coding of symbols according to composition, as in table 1.

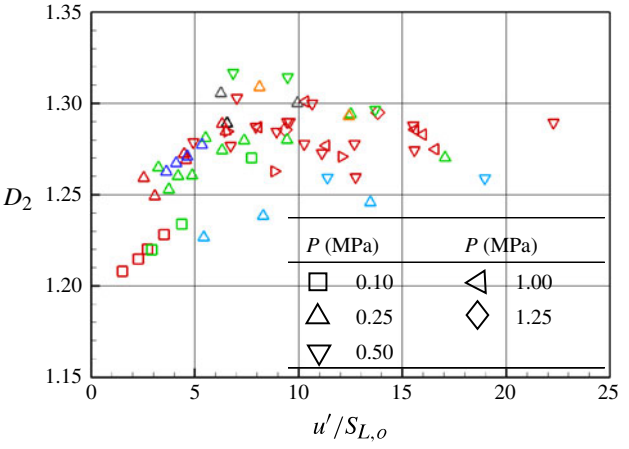


FIGURE 16. Fractal dimension as a function of $u'/S_{L,o}$. Colour-coding of symbols according to composition, as in table 1.

all measured flames are reported in figure 16, highlighting that $D_2$ increases initially with rising $u'/S_{L,o}$ and then levels off. The results corroborate other measurements performed mainly on hydrocarbons (Mantzaras *et al.* 1989; North & Santavicca 1990; Takeno *et al.* 1990; Gulder *et al.* 2000; Kobayashi & Kawazoe 2000). The hydrogen flames are apparently characterized by lower values of $D_2$; however, this result does not imply a lower degree of corrugation for these flames. It is in fact inappropriate to compare different fuels in this diagram, as the laminar flame speeds of the different generated flames can be very different from the unstretched $S_{L,o}$, depending on the specific fuel compositions. This topic will be fully addressed in the following §§ 4.3 and 4.4.

Figure 17 presents the statistics of $D_2$ and $\varepsilon_o$ for a single flame obtained with 400 single-shot realizations ($H_2$–CO/50–50, $P = 0.10$ MPa, $T_o = 623$ K, $U_o = 40$ m s$^{-1}$,

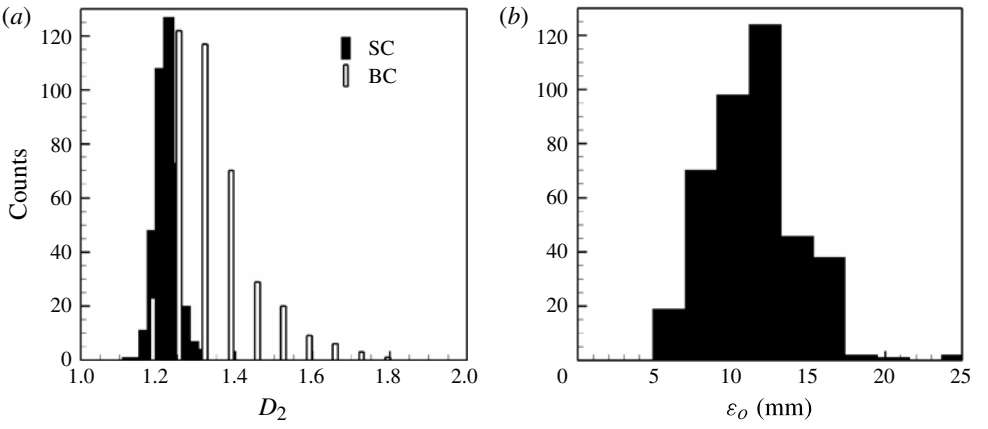


FIGURE 17. Histograms of $D_2$ and $\varepsilon_o$ ($H_2$–CO/50–50, $P = 0.10$ MPa, $T_o = 623$ K, $U_o = 40$ m s$^{-1}$, $\Phi = 0.41$, representing statistics of flame no. 9 in table 1).

$\Phi = 0.41$, flame no. 9 in table 1). The histograms in figure 17(*a*) provide the distributions of $D_2$ as extracted with the SC and BC methods; a Gaussian narrow-banded distribution is evident for the SC analysis, while the BC method exhibits a higher standard deviation. The inaccuracy of the BC method coupled with the intrinsic small variation of the fractal parameters makes the choice of SC imperative for the evaluation of turbulent flame speed data.

The standard deviation of the SC method need not be interpreted as an experimental uncertainty, but it is representative of the shot-to-shot variation characteristics of the different flame realizations.

### 4.3. *Comparison of global consumption and mean fractal-deduced consumption*

Normalized turbulent flame speed data obtained from (3.2) as described in Daniele *et al.* (2009, 2011) along with $S_T/S_{L,o}$ and $S_T/S_{L,k}$ extracted from (3.3) and (3.4), are compared in this section. $S_{L,k}$ is to be understood as the average propagation velocity of all the flamelets constituting the flame front. Differences between $S_T/S_{L,k}$ and $S_T/S_{L,o}$ reflect differences between $S_{L,k}$ and $S_{L,o}$, which are a measure of the interaction between stretch and PDT effects, as also discussed in Lipatnikov & Chomiak (2010).

Before comparing data derived with the two analyses ((3.2) versus (3.3) and (3.4)), it is important to clarify the significance of the two obtained results and their differences. For a given operating condition, the instantaneous flame front moves chaotically within the brush thickness and assumes different flame speeds associated with its position and the resulting flame front area. A progress variable $c$, defined within the flame brush thickness, describes the distribution of such flame positions. Daniele *et al.* (2011) presented only $S_T$ data associated with $\langle c \rangle = 0.05$ ($S_T^{0.05}$). The speed $S_T^{0.05}$ represents a consumption speed higher than the corresponding values for 95 % of the flame fronts in the brush thickness and smaller than the corresponding value of the remaining 5 % flame fronts.

When applying the fractal analysis in (3.4) to close (3.3), fractal parameters were extracted for 400 flame fronts representative of the full range of the flame brush. Therefore, for every operating condition, only the highest values of the $S_T/S_{L,k}$ distribution (derived via (3.3) and (3.4)) could effectively compare with $S_T^{0.05}$ derived

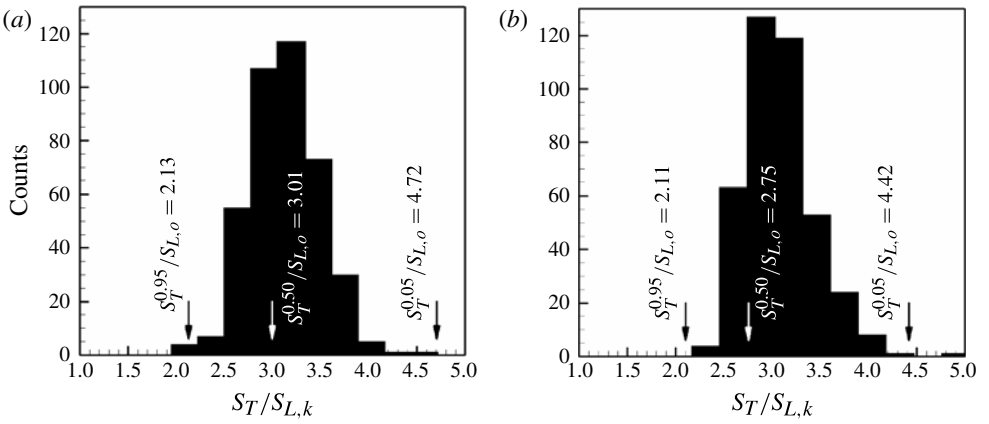


FIGURE 18. Comparison of results obtained with (3.2)–(3.4) for $CH_4$. Mean values of the $S_T/S_{L,k}$ distributions are (*a*) 3.09 and (*b*) 3.04. Here $P = 0.25$ MPa, $T_o = 623$ K, $U_o = 40$ m s$^{-1}$, $\Phi = 0.71$ (*a*) and $\Phi = 0.62$ (*b*), flames no. 1 and no. 2 in table 1.

from (3.2). Consequently, the mean value of $S_T/S_{L,k}$ better compares with $S_T$ derived on the $\langle c \rangle = 0.50$ progress variable ($S_T^{0.50}$).

Comparison of two $CH_4$ flames ($P = 0.25$ MPa, $T_o = 623$ K, $U_o = 40$ m s$^{-1}$, $\Phi = 0.62$ and 0.71, flames no. 1 and no. 2 in table 1) is shown in figure 18 where the fractal-analysis-derived $S_T/S_{L,k}$ distribution is plotted together with three values of $S_T/S_{L,o}$ associated with three progress variables $\langle c \rangle = 0.05$, 0.50 and 0.95, $S_T^{0.05}/S_{L,o}$, $S_T^{0.50}/S_{L,o}$ and $S_T^{0.95}/S_{L,o}$, respectively. The comparisons show very good agreement: differences between $S_T^{0.50}/S_{L,o}$ and the mean values of the fractal-derived distributions of $S_T/S_{L,k}$ are at most 10 % and are indicative of the small stretch effects on the laminar burning rate of methane fuels. These effects, for all stoichiometries of methane fuels investigated in the present work, turn out to be weak, as also reported in the methane studies of Renou & Boukhalfa (2001) and Chen (2011).

To simplify notation, the superscript 0.50 is dropped from $S_T^{0.50}/S_{L,o}$, and $S_T/S_{L,k}$ will henceforth denote the mean value of the fractal-based measured distribution. In the following, only the last two quantities will be compared. It is worth mentioning that $\langle c \rangle = 0.50$ was also used by Venkateswaran *et al.* (2011) to define the average flame area in recent atmospheric-pressure syngas and methane Bunsen flame experiments; this choice was again dictated by the need to compare turbulent consumption speeds with turbulent flame speed data obtained by other methodologies based on an equivalent $\langle c \rangle = 0.50$ definition, such as the mean flame angle method (Kobayashi *et al.* 1996).

To give a general overview, comparison of the results from the two analyses (global consumption and mean consumption) is now presented in terms of mean values of $S_T/S_{L,k}$ against $S_T/S_{L,o}$ in figure 19. Methane data points nearly lie on a line with unity slope (dashed line in figure 19), as anticipated from the result in figure 18. $H_2$-containing fuels are characterized by a higher $S_{L,k}$ than $S_{L,o}$ and therefore smaller $S_T/S_{L,k}$ compared with $S_T/S_{L,o}$. The last result quantitatively confirms the importance of the combination of stretch effects with PDT in enhancing the flamelet consumption speed ($S_{L,k}$) for $H_2$-containing fuels; this enhancement is especially important at high pressures (see figure 19).

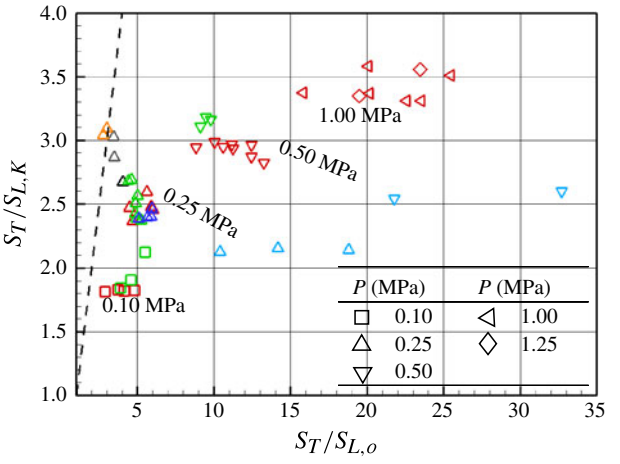


FIGURE 19. General comparison of results obtained with (3.2) ($S_T/S_{L,o}$) and (3.3)–(3.4) ($S_T/S_{L,k}$). Colour-coding of symbols according to composition, as in table 1.

The flame characteristics have been assessed by two-dimensional laser cuts. Nonetheless, (Chakraborty *et al.* 2011) reported that, despite growing deviations between the two-dimensional and three-dimensional probability density function (p.d.f.) shapes of the displacement speed with increasing $u'$, the corresponding mean values changed only modestly.

### 4.4. *Mean flamelets speed*

The mean flamelets speed or stretched laminar flame speed $S_{L,k}$ can be derived as follows:

$$S_{L,k} = \frac{(S_T)}{(S_T/S_{L,k})}, \tag{4.1}$$

where $S_T$ in the numerator is derived from (3.2) at $\langle c \rangle = 0.50$ and $S_T/S_{L,k}$ in the denominator is derived from (3.3) and (3.4). It is noted that $S_{L,k}$ has been extracted in this way for the first time.

In figures 20 and 21 stretched flamelet speeds normalized by the unstretched laminar speed, $S_{L,k}/S_{L,o}$, are presented versus the dimensional stretch $\kappa/S_{L,o}$, highlighting the effects of pressure and hydrogen content. This representation has the advantage of furnishing directly the Markstein length $l_M$, which corresponds to the growth rates (slope of the lines) in the provided diagrams according to the linear theory by Clavin (1985):

$$S_{L,k} = S_{L,o} - l_M \cdot \kappa, \tag{4.2}$$

where $l_M$ is the Markstein length.

The normalized stretch $\kappa$, induced by the turbulence field, can be estimated as follows:

$$\kappa = \frac{u'}{\lambda}, \tag{4.3}$$

with the Taylor scale, $\lambda$, derived using isotropic turbulence relations (Pope 2001).

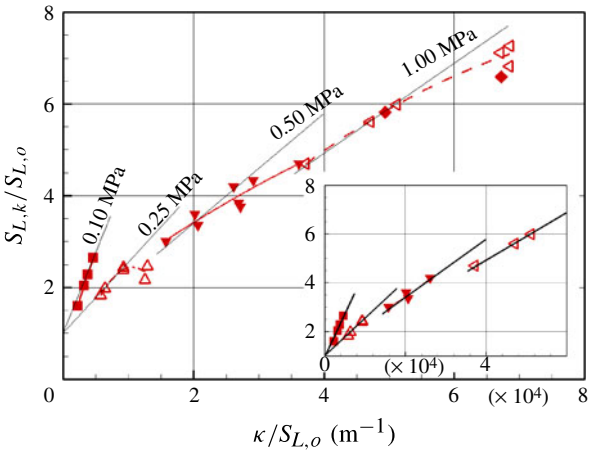


FIGURE 20. Effect of stretch on flamelets speed for a fuel mixture with $H_2$–CO/50–50. The inset provides the data subset for which $u'/S_{L,k} < 2.15$.

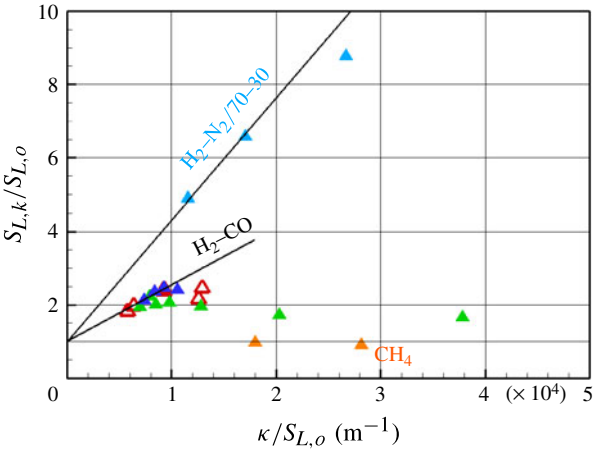


FIGURE 21. Effect of stretch on flamelets speed for fixed pressure ($P = 0.25$ MPa). Colour-coding of symbols according to composition, as in table 1.

In figure 20, the effect of pressure on $S_{L,k}/S_{L,o}$ is depicted for a constant mixture composition ($H_2$–CO/50–50), while in figure 21 the effect of fuel composition is highlighted for a constant pressure of 0.25 MPa. The curves in these diagrams show an initial linear growth, extrapolated to $S_{L,k}/S_{L,o} = 1$ for $\kappa/S_{L,o} = 0$. This is in agreement with the linear theory (Clavin 1985) reported in (4.2). This behaviour has already been described in various studies by using the *Ka* number, stretch and normalized stretch (for example in Renou & Boukhalfa (2001), Bradley *et al.* (2007) and Weiss *et al.* (2008)) with the difference that most of the literature studies were based on expanding flames where stretch was defined according to the radius of the spherical flame.

With increasing $\kappa/S_{L,o}$, the curves exhibit a bending behaviour. Bending occurs at high values of $u'/S_{L,k}$, while a linear behaviour can be seen in the inset of figure 20 for selected data satisfying $u'/S_{L,k} < 2.15$. The bending effect is a function of the

parameter selected to evaluate the stretch, which here is $u'/\lambda$. In fact, the normalized turbulence intensity can be understood as follows:

$$\frac{u'}{S_{L,k}} = \frac{u'}{\lambda} \cdot \frac{\lambda}{S_{L,k}} = \kappa \cdot \tau_{c,\lambda}, \tag{4.4}$$

suggesting that the aforementioned bending is a result of competition between two time scales:

(*a*) the inverse of $\kappa = u'/\lambda$ which is proportional to the turnover time of the smallest eddies interacting with the flame front (since $\lambda$, $\delta_L$ and $\varepsilon_i$ are of the same order of magnitude);

(*b*) $\tau_{c,\lambda} = \lambda/S_{L,k}$, which is the propagation time of the flamelets at the smallest scale of wrinkling (again because $\lambda$, $\delta_L$ and $\varepsilon_i$ have the same order of magnitude).

The parameter $u'/\lambda$ is representative of the stretch rate only if the flame front can fully interact with the turbulent eddies and can adapt its shape accordingly. This is apparently the case for low values of $u'/S_{L,k}$. When this parameter exceeds a certain threshold value, the flame front cannot follow such eddies because of its long characteristic time $\tau_{c,\lambda}$. Therefore, the effective stretch induced by $u'/\lambda$ which is experienced by the flame front is reduced. Consequently, PDT effects couple with a smaller effective stretch rate yielding lower values for $S_{L,k}/S_{L,o}$ at high $u'/S_{L,k}$.

In figure 21, $CH_4$ data points are characterized by $S_{L,k}/S_{L,o} \approx 1$ while $H_2$–$N_2$ data exhibit the highest values. The $H_2$–CO mixtures at three different compositions show a similar trend, revealing a quasi-independence of PDT characteristics on the specific $H_2$ to CO ratio. It has to be underlined that the $H_2$–$N_2$ mixture has a considerably higher $l_M$ when compared with the examined syngas mixtures, which have a highest $H_2$ volumetric content of 67 %. This demonstrates the important role of CO in inhibiting the PDT characteristics of the fuel mixture.

Markstein lengths, $l_M$, extracted from the fitted lines in figure 20 are plotted in figure 22 and illustrate the pressure dependence of this parameter. These lengths represent an average of the values derived from (4.2) (when applied to the interpolated points shown in the inset of figure 20). In the same diagram, the laminar flame thicknesses $\delta_L$ and $\overline{Ma}$ numbers ($\overline{Ma} = l_M/\delta_L$) for two stoichiometries of 0.42 and 0.45 are also reported. The Markstein length $l_M$ grows with pressure but the decay of the laminar flame thickness $\delta_L$ has a higher absolute pressure exponent. The combined effect leads to average $\overline{Ma}$ numbers exhibiting a linear dependence on $P$ with negative slope. The negative growth of $\overline{Ma}$ with pressure demonstrates the increased coupling between DL and PDT instabilities at elevated pressures.

The drop of the Markstein number with rising pressure in figure 22 has also been shown theoretically in Creta & Matalon (2011); moreover, this drop is consistent with $S_T$ correlations having power-law pressure dependencies with positive exponents Kobayashi *et al.* (2005) and Daniele *et al.* (2011). Average Markstein numbers derived using (4.2) are presented in figure 23 for different fuel mixtures and for a constant pressure of 0.25 MPa. Markstein numbers are nearly zero for $CH_4$, as also found in Chen (2011), Renou & Boukhalfa (2001) and Weiss *et al.* (2008), and assume small negative values for $CH_4$ + syngas mixtures. The very good agreement with the extensive methane literature regarding the nearly zero Markstein number of this fuel attests the aptness of our applied methodology. Pure syngas mixtures and $H_2$ (with $N_2$ dilution) are characterized by strongly negative values. The higher the $H_2$ content, the lower $\overline{Ma}$ is. The negative growth of $\overline{Ma}$ shown in figure 23 has already been observed by other authors (Renou & Boukhalfa 2001; Lamoureux *et al.* 2003; Bradley *et al.*

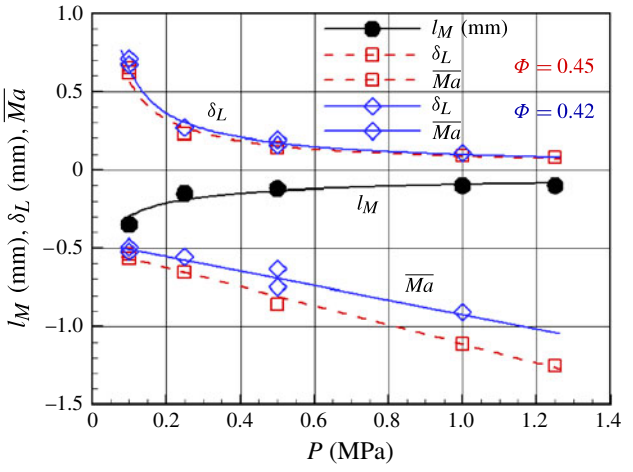


FIGURE 22. Pressure effect on average Markstein numbers ($\overline{Ma}$) and lengths ($l_M$) ($H_2$–CO/50–50).

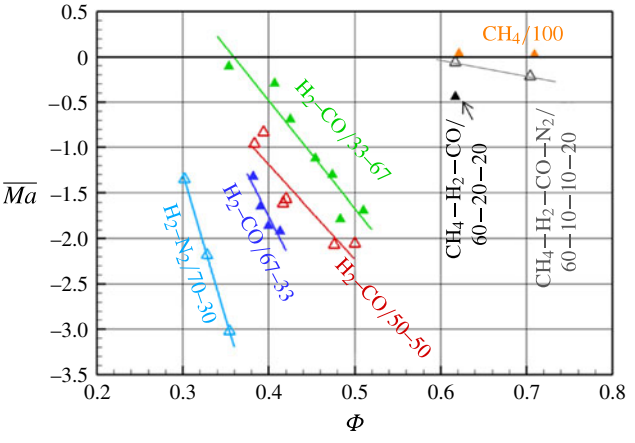


FIGURE 23. Equivalence ratio and fuel effect on average Markstein number $\overline{Ma}$ ($P = 0.25$ MPa).

2007; Weiss *et al.* 2008; Chen 2011) within the range of $\Phi$ which is presented here but only for pure $H_2$ flames. The negative growth implies an increasing coupling of PDT and stretch effects.

The data in figures 22 and 23 on Markstein lengths and numbers for syngas mixtures are reported for the first time in the literature. Comparisons of $\overline{Ma}$ and $l_M$ with literature values for pure hydrogen is outside of the scope of this work, as these parameters depend on many arbitrary choices like definition of unburned and burned $\overline{Ma}$ numbers and $l_M$, and definitions of $Ka$, laminar flame thickness, stretch rate, Taylor scales, etc. All of these choices make it difficult if not impossible to recalculate $\overline{Ma}$ numbers and $l_M$ proposed by other authors for comparison with our results. However, the behaviour shown in figures 22 and 23 provides a clear quantitative picture of the importance of the coupling between stretch effects and PDT for different fuels.

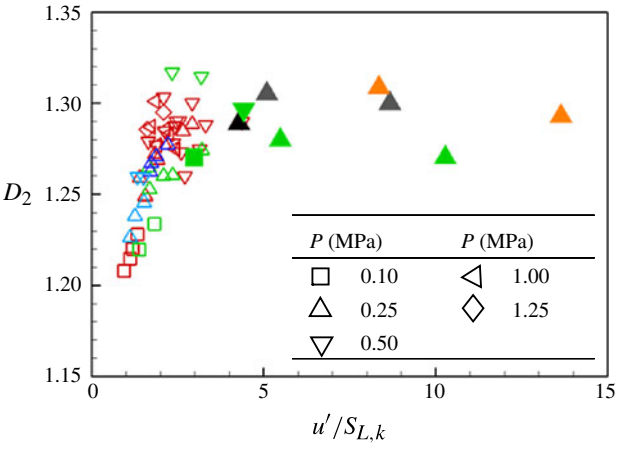


FIGURE 24. Dependence of fractal dimension $D_2$ on $u'/S_{L,k}$. Colour-coding of symbols according to composition, as in table 1.

The trend of decreasing (negatively) Markstein numbers with increasing equivalence ratio in figure 23 is finally consistent with laminar stretched flame investigations. Aung, Hassan & Faeth (1997) and Bradley *et al.* (2007) have reported decreasing (negatively) *Ma* for lean $H_2$/air flames with $\varphi \leqslant 0.50$; however, for $\varphi > 0.60$ both aforementioned works find that *Ma* increases with rising $\varphi$ .

### 4.5. *Flame front/eddies interaction*

To fully address the propagation of a flame front in a turbulent field, besides understanding the flamelets velocity $S_{L,k}$, knowledge of the interaction between eddies and flame front is of fundamental importance. This interaction determines the turbulent flame speed and has been addressed in our earlier work for syngas fuels and methane (Daniele *et al.* 2011). Therein, we proposed that this interaction reflects the fact that a given flame front can couple with eddies having a comparable temporal activity to that of the flame front itself. In order to give an analytic representation, two time scales were defined: the turnover time of the eddies of the integral scale ($\tau_f = L_T/u'$) and the time response of the flame front, defined as the flame brush thickness over turbulent flame speed ($\tau_c = f_{BT}/S_T$). We demonstrated that when these two scales differ by an order of magnitude ($\tau_c \approx 10\tau_f$) the flame front/turbulent eddies interaction becomes weak. For these conditions, turbulent eddies corrugate the flame front to a partial extent only and data points exhibit the classical bending characteristic ($S_T/S_L$ versus $u'/S_L$). The same information can be derived from the fractal dimension in figure 24, plotted versus $u'/S_{L,k}$. The criterion $\tau_c = 10\tau_f$ partitions the data points into two different sets: the first set characterized by a nearly linear increase of $D_2$ (open symbols) and a second set of data for which $D_2$ flattens out and remains fairly constant (filled symbols). The plateau value $D_2 \approx 1.3$ in figure 24 is consistent with earlier experiments (Mantzaras *et al.* 1989; North & Santavicca 1990) and is close to the value of 1.23 obtained theoretically by Creta, Fogla & Matalon (2011). It is thus demonstrated again, with direct measurements of the flame front corrugation that, when the eddy temporal activity exceeds the time response of the flame, an increase in turbulence intensity is not followed by a proportional increase in flame front corrugation and thus data points show the classical bending behaviour. It is also

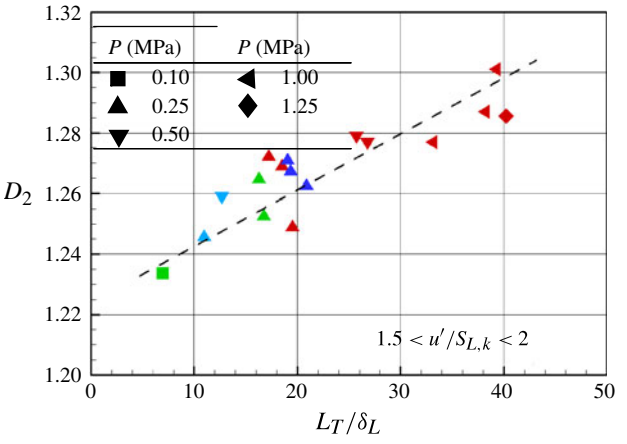


FIGURE 25. Dependence of fractal dimension $D_2$ on $L_T/\delta_L$. Colour-coding of symbols according to composition, as in table 1.

noted that while past studies have used spectral considerations to expose the effect of various time scales on the resulting flame corrugations (Sivashinsky 1988; Poinsot, Veynante & Candel 1991; Mantzaras 1992) none has reported a partitioning criterion similar to that presented above.

Figure 24 also highlights that $D_2$ is nearly fuel-independent. Thus, the PDT effects acting for $H_2$ fuels are not as effective in producing additional flame front area via an enhanced corrugation, at least for the values of $u'/S_{L,k}$ investigated in this work.

Figure 25 provides the dependence of $D_2$ on $L_T/\delta_L$ for a narrow range of normalized turbulence intensity. $D_2$ increases with increasing $L_T/\delta_L$ in a linear fashion. This effect is mostly attributed to the decrease in $\delta_L$, as this parameter varies stronger than $L_T$ for the present experiments. The behaviour in figure 25 is a direct consequence of the DL instability, which is more effective in corrugating the thinner higher-pressure flame fronts (Sivashinsky 1983; Law *et al.* 2005).

Summarizing, the fractal dimension $D_2$ is also a measure of the capacity of a given turbulent flow field to interact with a flame front, which is maximized by increasing $L_T/\delta_L$ and $u'/S_{L,k}$. This interaction is nonetheless limited by temporal coupling effects, which can be described with the characteristic times of the turbulent eddies and the flame front. The described dependencies have a nearly fuel-independent character.

### 4.6. $S_T/S_L$: *pressure and fuel effect*

Normalized turbulent flame speed data derived with the fractal analysis (equations (3.3) and (3.4)) are presented in figure 26 versus $u'/S_{L,k}$ for three different pressures and for all investigated fuels.

The figure reveals the effect of pressure in enhancing the normalized burning rate, which is usually attributed to DL instabilities. This effect was already discussed by Daniele *et al.* (2011), where $S_T$ data were normalized with $S_{L,o}$, since $S_{L,k}$ was unavailable. However, in the work of Daniele *et al.* (2011) different fuels could not be grouped together in the simple $S_T/S_{L,o}$ versus $u'/S_{L,o}$ diagram. With the introduction of $S_{L,k}$, data at the same pressure can be fitted on a single curve despite the different fuel compositions. This is an important result of this investigation, suggesting that, for the levels of $u'/S_L$ examined here, preferential diffusion of $H_2$ does not trigger an

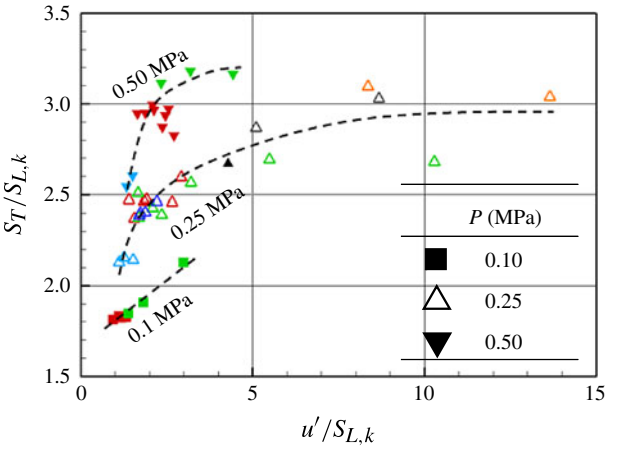


FIGURE 26. Normalized $S_T$ versus normalized $u'$. Colour-coding of symbols according to composition, as in table 1.

enhanced flame front corrugation and thus does not contribute to a substantial growth in the flame front surface but acts predominantly on the flamelets propagation velocity $S_{L,k}$. The effect of pressure shown in figure 26, predominantly contains DL effects, as the PDT effects are taken into account by the normalization with $S_{L,k}$.

## 5. Conclusions

Turbulent flame speeds ($S_T$) and stretched laminar flame speeds, $S_{L,k}$, have been measured in recirculation-stabilized axisymmetric flames at pressures up to 1.25 MPa, preheat temperatures of 623 K and ratios of turbulence intensities to unstrained laminar flame speeds, $u'/S_{L,o}$, up to 30. Investigated fuels included pure methane, syngas ($H_2$–$CO_2$ blends with molar ratios ranging from 33/67 to 67/33), mixtures of methane and syngas, and finally pure hydrogen. Measurements involved PLIF of the OH radical for assessing the flame front corrugation and PIV for characterizing the turbulent flow field. Flame images were simultaneously acquired at both low and high resolutions so as to investigate flame propagation characteristics at the large and small scales, respectively. Key conclusions of this study are as follows.

(*a*) Two different analysis techniques, a global one based on mass continuity and an average one based on fractal analysis, have been successfully employed for the first time to deduce absolute values of turbulent flame speeds and normalized turbulent flame speeds ($S_T/S_{L,k}$), respectively, for various syngas mixtures of interest to gas-turbine combustion technologies.

(*b*) For the flame front fractal analysis, a new algorithm has been proposed on the SC approach that largely removes inherent limitations of the method and minimizes the resulting standard deviations. Analyses in known fractal calibration curves have shown that fractal dimensions and outer cutoffs can be determined accurately.

(*c*) The impact of hydrodynamic (DL) and preferential thermal diffusion (PDT) effects on the flame propagation characteristics has been investigated. Hydrogen-containing fuels are characterized by $S_{L,k}$ larger than $S_{L,o}$, indicating the importance of the combination of stretch with PDT effects in enhancing the average flamelet

consumption speed. Moreover, this enhancement is accentuated at higher pressures, suggesting increased coupling of PDT with DL effects.

(*d*) Within the range of examined $H_2$ content in the syngas (from 33 to 67 % by volume), the impact of hydrogen addition in CO did not result in markedly different response for the $S_{L,k}/S_{L,o}$ ratios. This result suggested that the presence of CO moderated the PDT effects of hydrogen.

(*e*) Average Markstein numbers ($\overline{Ma}$) and lengths have been deduced for the examined reactive mixtures. While $\overline{Ma}$ numbers for pure $CH_4$ fuels were practically zero, in agreement with literature data, $\overline{Ma}$ numbers for $H_2$-containing fuels increased (in absolute value) with increasing $H_2$ content. Moreover, the growth of the absolute value of $\overline{Ma}$ numbers with rising pressure demonstrated an increasing coupling of the DL and PDT instabilities.

(*f*) Normalized $S_T/S_{L,k}$ versus $u'/S_{L,k}$ plots, as well as the fractal dimension $D_2$ versus $u'/S_{L,k}$ plots were largely independent of fuel composition (and thus hydrogen content) indicating that PDT effects acted primarily on enhancing the average stretched flame propagation speed $S_{L,k}$ rather than on increasing the flame corrugation and thus the flame area.

(*g*) All examined cases were in the thin reaction zones regime. The laminar flame thicknesses, Taylor scales and inner cutoffs were of roughly the same magnitude. Based on the size proximity of these scales, the bending of the $S_T/S_{L,k}$ versus $u'/S_{L,k}$ plots and of the $D_2$ versus $u'/S_{L,k}$ plots with increasing $u'/S_{L,k}$ could be explained using a temporal scale analysis, by comparing turnover turbulent eddy times with flame transit times.

*Nomenclature*

| | |
|---|---|
| $A_o, A_{in,j}, A_{av}$ | Inlet, instantaneous, and average flame areas ($m^2$), figure 6 |
| $c$ | Progress variable (−) |
| $D_2$ | Fractal dimension (−), (3.4) |
| $Da$ | Damköhler number (−), figure 5 |
| $f_{BT}$ | Turbulent flame brush thickness (m), table 1 |
| $Ka$ | Karlovitz number (−) |
| $L_T$ | Integral length scale (m) |
| $l_M$ | Markstein length (m), (4.2) |
| $Le^*$ | Effective Lewis number of mixture, table 1 |
| $\overline{Ma}$ | Average Markstein number (−), $l_M/\delta_L$ |
| $P$ | Pressure (Pa) |
| $Re_T$ | Turbulence Reynolds number (−), $u'L_T/\nu$ |
| $S_{L,o}$ | Unstretched laminar flame speed ($m\ s^{-1}$) |
| $S_{L,k}$ | Average stretched laminar flame speed ($m\ s^{-1}$) |
| $S_T$ | Turbulent flame speed ($m\ s^{-1}$) |
| $S_T^{0.50}$ | Turbulent flame speed at the $\langle c \rangle = 0.50$ isosurface ($m\ s^{-1}$) |
| $T_o$ | Preheat temperature (K) |
| $U_o$ | Inlet velocity ($m\ s^{-1}$) |
| $u'$ | Turbulence intensity ($m\ s^{-1}$) |

*Greek letters*

| | |
|---|---|
| $\delta_L$ | Thickness of unstretched laminar flame (m) |
| $\varepsilon_i$, $\varepsilon_o$ | Inner and outer cutoff scales (m), (3.4) |
| $\eta$ | Kolmogorov scale of turbulence (m) |
| $\kappa$ | Stretch rate ($s^{-1}$) |
| $\lambda$ | Taylor length scale (m) |
| $\nu$ | Molecular kinematic viscosity ($m^2\ s^{-1}$) |
| $\Phi$ | Fuel-to-air equivalence ratio (−) |

## Acknowledgements

We gratefully acknowledge the financial support of this research by the Swiss Federal Office of Energy (BFE) and Alstom Power Switzerland. We thank Mr D. Erne for supporting the experimental campaign and Dr P. Siewert for the PIV data.

## REFERENCES

APPEL, C., MANTZARAS, J., SCHAEREN, R., BOMBACH, R. & INAUEN, A. 2005 Turbulent catalytically stabilized combustion of hydrogen/air mixtures in entry channel flows. *Combust. Flame* **140**, 70–92.

AUNG, K. T., HASSAN, M. I. & FAETH, G. M. 1997 Flame stretch interactions of laminar premixed hydrogen/air flames at normal temperature and pressure. *Combust. Flame* **109**, 1–24.

BAUM, M., POINSOT, T. J., HAWORTH, D. C. & DARAHIBA, N. 1994 Direct numerical simulation of $H_2/O_2/N_2$ flames with complex chemistry in two-dimensional turbulent flows. *J. Fluid Mech.* **281**, 1–32.

BELL, J. B., CHENG, R. K., DAY, M. S. & SHEPHERD, I. G. 2007 Numerical investigation of Lewis number effects on lean premixed turbulent flames. *Proc. Combust. Inst.* **31**, 1309–1317.

BRADLEY, D. 1992 How fast can we burn?. *Proc. Combust. Inst.* **24**, 247–262.

BRADLEY, D., LAWES, M., LIU, K., VERHELST, S. & WOOLLEY, R. 2007 Laminar burning velocities of lean hydrogen–air mixtures at pressures up to 1.0 MPa. *Combust. Flame* **149**, 162–172.

CANTERA, 1998 www.cantera.org.

CHAKRABORTY, N. & CANT, R. S. 2011 Effect of Lewis number on flame surface density transport in turbulent premixed combustion. *Combust. Flame* **158**, 1768–1787.

CHAKRABORTY, N., HARTUNG, G., KATRAGADDA, M. & KAMINSKI, C. F. 2011 Comparison of 2D and 3D density-weighted displacement speed statistics and implications for laser based measurements of flame displacement speed using direct numerical simulation data. *Combust. Flame* **158**, 1372–1390.

CHAOS, M. & DRYER, F. L. 2008 Syngas combustion kinetics and applications. *Combust. Sci. Technol.* **180**, 1053–1096.

CHEN, Z. 2011 On the extraction of laminar flame speed and Markstein length from outwardly propagating spherical flames. *Combust. Flame* **158**, 291–300.

CHEN, Y. C. & MANSOUR, M. S. 1999 Topology of turbulent premixed flame fronts resolved by simultaneous planar imaging of LIPF of OH radical and Rayleigh scattering. *Exp. Fluids* **26**, 277–287.

CHENG, R. K. 2009 Turbulent combustion properties of premixed syngas. In *Synthesis Gas Combustion – Fundamentals and Applications* (ed. T. Lieuwen, V. Yang & R. Yetter), pp. 129–168. CRC.

CLAVIN, P. 1985 Dynamic behavior of premixed flame fronts in laminar and turbulent flows. *Prog. Energy Combust. Sci.* **11**, 1–59.

COHE, C., HALTER, F., CHAUVEAU, C., GOKALP, I. & GULDER, O. L. 2007 Fractal characterisation of high-pressure and hydrogen-enriched $CH_4$–air turbulent premixed flames. *Proc. Combust. Inst.* **31**, 1345–1352.

CRETA, F., FOGLA, N. & MATALON, M. 2011 Turbulent propagation of premixed flames in the presence of Darrieus–Landau instability. *Combust. Theor. Model.* **15**, 267–298.

CRETA, F. & MATALON, M. 2011 Propagation of wrinkled turbulent flames in the context of hydrodynamic theory. *J. Fluid Mech.* **680**, 225–264.

DANIELE, S., JANSOHN, P. & BOULOUCHOS, K. 2009 Flame front characteristic and turbulent flame speed of lean premixed syngas combustion at gas turbine relevant conditions. *Proc. ASME Turbo Expo. 2009*, **2**, 393–400.

DANIELE, S., JANSOHN, P., MANTZARAS, J. & BOULOUCHOS, K. 2011 Turbulent flame speed for syngas at gas turbine relevant conditions. *Proc. Combust. Inst.* **33**, 2937–2944.

FOROUTAN-POUR, K., DUTILLEUL, P. & SMITH, D. L. 1999 Advances in the implementation of the box-counting method of fractal dimension estimation. *Appl. Math. Comput.* **105**, 195–210.

GOULDIN, F. C., BRAY, K. N. C. & CHEN, J. Y. 1989 Chemical closure-model for fractal flamelets. *Combust. Flame* **77**, 241–259.

GRIEBEL, P., BOMBACH, R., INAUEN, A., KREUTNER, W. & SCHAEREN, R. 2002 Structure and NO emission of turbulent high pressure lean premixed methane/air flames. In *Proceedigns of 6th European Conference on Industrial Furnaces and Boilers*, pp. 45–54. INFUB.

GU, X. J., HAQ, M. Z., LAWES, M. & WOOLLEY, R. 2000 Laminar burning velocity and Markstein lengths of methane–air mixtures. *Combust. Flame* **121**, 41–58.

GULDER, O. L. & SMALLWOOD, G. J. 1995 Inner cutoff scale of flame surface wrinkling in turbulent premixed flames. *Combust. Flame* **103**, 107–114.

GULDER, O. L., SMALLWOOD, G. J., WONG, R., SNELLING, D. R., SMITH, R., DESCAMPS, B. M. & SAUTET, J. C. 2000 Flame front surface characteristics in turbulent premixed propane/air combustion. *Combust. Flame* **120**, 407–416.

HOFFMANN, S., BARTLETT, M., FINKENRATH, M., EVULET, A. & URSIN, T. P. 2009 Performance and cost analysis of advanced gas turbine cycles with precombustion $CO_2$ Capture. *Trans. ASME: J. Engng Gas Turbines Power* **131**, 021701.

HUANG, Z., ZHANG, Y., ZENG, K., LIU, B., WANG, Q. & JIANG, D. M. 2006 Measurements of laminar burning velocities for natural gas–hydrogen–air mixtures. *Combust. Flame* **146**, 302–311.

ICHIKAWA, Y., OTAWARA, Y., KOBAYASHI, H., OGAMI, Y., KUDO, T., OKUYAMA, M. & KADOWAKI, S. 2011 Flame structure and radiation characteristics of $CO/H_2/CO_2$/air turbulent premixed flames at high pressure. *Proc. Combust. Inst.* **33**, 1543–1550.

KOBAYASHI, H. & KAWAZOE, H. 2000 Flame instability effects on the smallest wrinkling scale and burning velocity of high-pressure turbulent premixed flames. *Proc. Combust. Inst.* **28**, 375–382.

KOBAYASHI, H., OTAWARA, Y., WANG, J., MATSUNO, F., OGAMI, Y., OKUYAMA, M., KUDO, T. & KADOWAKI, S. 2013 Turbulent premixed flame characteristics of a $CO/H_2/O_2$ mixture highly diluted with $CO_2$ in a high-pressure environment. *Proc. Combust. Inst.* **34**, 1437–1445.

KOBAYASHI, H., SEYAMA, K., HAGIWARA, H. & OGAMI, Y. 2005 Burning velocity correlation of methane/air turbulent premixed flames at high pressure and high temperature. *Proc. Combust. Inst.* **30**, 827–834.

KOBAYASHI, H., TAMURA, K., MARUTA, K., NIIOKA, & WILLIAMS, F. A. 1996 Burning velocity of turbulent premixed flames in a high-pressure environment. *Proc. Combust. Inst.* **26**, 389–396.

KWON, O. C. & FAETH, G. M. 2001 Flame/stretch interactions of premixed hydrogen-fueled flames: measurements and predictions. *Combust. Flame* **124**, 590–610.

LACHAUX, T., HALTER, F., CHAUVEAU, C., GÖKALP, I. & SHEPHERD, I. G. 2005 Flame front analysis of high-pressure turbulent lean premixed methane–air flames. *Proc. Combust. Inst.* **30**, 819–826.

LAMOUREUX, N., DJEBAILI-CHAUMEIX, N. & PAILLARD, C. E. 2003 Laminar flame velocity determination for $H_2$–air–He–$CO_2$ mixtures using the spherical bomb method. *Exp. Therm. Fluid Sci.* **27**, 385–393.

LANDAU, L. 1944 On the theory of slow combustion. *Acta Physicochim. USSR* **19**, 77–85.

LAW, C. K., JOMAAS, G. & BECHTOLD, J. K. 2005 Cellular instabilities of expanding hydrogen/propane spherical flames at elevated pressures: theory and experiment. *Proc. Combust. Inst.* **30**, 159–167.

LI, J., ZHAO, Z. W., KAZAKOV, A., CHAOS, M., DRYER, F. L. & SCIRE, J. J. 2007 A comprehensive kinetic mechanism for CO, $CH_2O$, and $CH_3OH$ combustion. *Intl J. Chem. Kinet.* **39**, 109–136.

LIN, Y.-C 2013 Hydrogen combustion for gas turbines applications (PhD thesis, ongoing), Swiss Federal Institute of Technology ETH-Zurich.

LIPATNIKOV, A. & CHOMIAK, J. 2005 Molecular transport effects on turbulent flame propagation and structure. *Prog. Energy Combust. Sci.* **31**, 1–73.

LIPATNIKOV, A. & CHOMIAK, J. 2010 Effects of premixed flames on turbulence and turbulent scalar transport. *Prog. Energy Combust. Sci.* **36**, 1–102.

MANDELBROT, B. B. 1985 Self-affine fractals and fractal dimension. *Phys. Scr.* **32**, 257–260.

MANTZARAS, J. 1992 Geometrical properties of turbulent premixed flames: comparison between computed and measured quantities. *Combust. Sci. Technol.* **86**, 135–162.

MANTZARAS, J., FELTON, P. G. & BRACCO, F. V. 1989 Fractals and turbulent premixed engine flames. *Combust. Flame* **77**, 295–310.

METGHALCHI, M. & KECK, J. C. 1980 Laminar burning velocity of propane–air mixtures at high-temperature and pressure. *Combust. Flame* **38**, 143–154.

NATARAJAN, J., LIEUWEN, T. & SEITZMAN, J. 2007 Laminar flame speeds of $H_2$/CO mixtures: effect of $CO_2$ dilution, preheat temperature, and pressure. *Combust. Flame* **151**, 104–119.

NORTH, G. L. & SANTAVICCA, D. A. 1990 The fractal nature of premixed turbulent flames. *Combust. Sci. Technol.* **72**, 215–232.

PETERS, N. 1999 The turbulent burning velocity for large-scale and small-scale turbulence. *J. Fluid Mech.* **384**, 107–132.

PETERSEN, B. R. & GHANDHI, J. B. 2009 High resolution scalar dissipation measurements in an IC engine. *SAE Intl J. Engines* **2**, 475–491.

POINSOT, T. & VEYNANTE, D. 2005 *Theoretical and Numerical Combustion*. R.T. Edwards.

POINSOT, T., VEYNANTE, D. & CANDEL, S. 1991 Quenching processes and premixed turbulent combustion diagrams. *J. Fluid Mech.* **228**, 561–606.

POPE, S. B. 2001 *Turbulent Flows*. Cambridge University Press.

RENOU, B. & BOUKHALFA, A. 2001 An experimental study of freely propagating premixed flames at various Lewis numbers. *Combust. Sci. Technol.* **162**, 347–370.

SCHELKIN, K. I. 1943 On combustion in turbulent flow. *Zh. Tekh. Fiz.* **13**, 520–530.

SHEPHERD, I. G., CHENG, R. K. & TALBOT, L. 1992 Experimental criteria for the determination of fractal parameters of premixed turbulent flames. *Exp. Fluids* **13**, 386–392.

SIEWERT, P. 2005 Flame front characteristics of turbulent premixed lean methane/air flames at high-pressure and high-temperature. PhD thesis, Swiss Federal Institute of Technology ETH-Zurich.

SIVASHINSKY, G. I. 1983 Instabilities, pattern-formation, and turbulence in flames. *Annu. Rev. Fluid Mech.* **15**, 179–199.

SIVASHINSKY, G. I. 1988 Cascade-renormalization theory of turbulent flame speed. *Combust. Sci. Technol.* **62**, 77–96.

SMITH, G. P., GOLDEN, D. M., FRENKLACH, M., MORIARTY, N. W., EITENEER, B., GOLDENBERG, M., BOWMAN, C. T., HANSON, R. K., SONG, S., GARDINER, W. C. JR., LISSIANSKI, V. V. & QUIN, Z. 2000 An optimized detailed chemical reaction mechanism for methane combustion. Gas Research Institute.

SOILLE, P. & RIVEST, J. F. 1996 On the validity of fractal dimension measurements in image analysis. *J. Vis. Commun. Image R.* **7**, 217–229.

SUNG, C. J. & LAW, C. K. 2008 Fundamental combustion properties of $H_2$/CO mixtures: ignition and flame propagation at elevated pressures. *Combust. Sci. Technol.* **180**, 1097–1116.

TAKENO, T., MURAYAMA, M. & TANIDA, Y. 1990 Fractal analysis of turbulent premixed flame surface. *Exp. Fluids* **10**, 61–70.

TOCK, L & MARECHAL, F. 2012 $H_2$ processes with $CO_2$ mitigation: thermo-economic modeling and process integration. *Intl J. Hydrogen Energy* **37**, 11785–11795.

VENKATESWARAN, P., MARSHALL, A., HYUK-SHIN, D., NOBBLE, D., SEITZMAN, J. & LIEUWEN, T. 2011 Measurements and analysis of turbulent consumption speeds of $H_2$/CO mixtures. *Combust. Flame* **158**, 1602–1614.

WEISS, M., ZARZALIS, N. & SUNTZ, R. 2008 Experimental study of Markstein number effects on laminar flamelet velocity in turbulent premixed flames. *Combust. Flame* **154**, 671–691.

YAKHOT, V. 1988 Propagation velocity of premixed turbulent flames. *Combust. Sci. Technol.* **60**, 191–214.

YUEN, F. T. C. & GÜLDER, Ö. L. 2013 Turbulent premixed flame front dynamics and implications for limits of flamelet hypothesis. *Proc. Combust. Inst.* **34**, 1393–1400.